The inclusion of scalar dissipation rate in modeling of an n-dodecane spray flame using flamelet generated manifold

Bao, Hesheng; Akargun, Hayri Yigit; Roekaerts, Dirk; Somers, Bart

DOI
10.1016/j.combustflame.2022.112610

Publication date
2023

Document Version
Final published version

Published in
Combustion and Flame

Combustion and Flame 249 (2023) 112610

Contents lists available at ScienceDirect

Combustion and Flame

journal homepage: www.elsevier.com/locate/combustflame

The inclusion of scalar dissipation rate in modeling of an *n*-dodecane spray flame using flamelet generated manifold

Hesheng Bao[a,*], Hayri Yigit Akargun[a], Dirk Roekaerts[a,b], Bart Somers[a]

[a] Department of Mechanical Engineering, Eindhoven University of Technology, the Netherlands
[b] Department of Process and Energy, Delft University of Technology, the Netherlands

ARTICLE INFO

Article history:
Received 10 May 2022
Revised 23 December 2022
Accepted 28 December 2022

Keywords:
ECN Spray A
Flamelet generated manifold
Ignition
Soot
Scalar dissipation rate

ABSTRACT

In this work, an extension of the Flamelet Generated Manifold (FGM) method is developed suitable for igniting turbulent flames. To create the FGM, the strongly stretched flamelet equations (SSFE) are solved. Whereas in the standard basic method a single representative flamelet strain rate is used, in the new method a range of strain rates is taken into account. This allows including the effect of a varying turbulent scalar dissipation rate (SDR) during ignition. The new approach is validated by applying it in an Large Eddy Simulation (LES) of the Engine Combustion Network (ECN) Spray A turbulent flame for which detailed experimental data are available. First, in a priori validation step, the performance of the new extended FGM, the multi-strainrate FGM (mFGM), is validated by the simulation of ignition and species profiles in laminar flames along the so-called S-curve diagram and comparing with full chemistry calculations. The sub-grid scale (SGS) spray dispersion model is validated against the inert spray experiments in terms of vapor and liquid penetration as well as the spatial distribution of mixture fraction and its root mean square. Finally, the performance of the extended FGM is evaluated by comparison with the ECN Spray A flame. It is found that compared to the single-strain-rate FGM, the prediction of the ignition delay is improved considerably. This is related to the effect of the inclusion of the effect of the SDR, which is mainly on the second-stage ignition, i.e. the high-temperature chemistry. The low-temperature combustion is also affected as it occurs in richer mixtures than observed for the single-strain-rate FGM. Especially the formaldehyde, associated with low-temperature combustion, occurs in wider distribution. Finally, also predictions of soot evolution are studied. To improve the soot prediction capabilities, a new correction to the retrieved source term of the important pre-cursor, acetylene, is introduced. The above modeling developments have been made using a customized OpenFOAM solver developed by the authors. This work demonstrates the importance of including the SSFE SDR as independent parameter in an FGM based on igniting flamelets.

1. Introduction

Internal combustion engines consume 70% of the world's fossil oil production [1] and continue to play a dominant role in the energy sector due to their high power density and robustness. The present paper pays attention to non-premixed diesel spray combustion due to its wide application in engines. Although many proposed innovations for Heavy-Duty and Marine applications investigate premixed combustion modes, most engines still involve non-premixed combustion. Its mixing-controlled flame development includes multiple time and length scales, and is a combination of jet breakup, evaporation, mixing and complex chemistry. This motivates investigations towards a deeper understanding of spray combustion fundamentals.

The combustion chamber is widely adopted to understand spray formation and combustion in engines. It applies an injection of high-pressure diesel-like fuel into well-defined ambient conditions. The ambient is created to mimic typical conditions for engines including fuel and oxidizer temperature, oxygen level, background pressure, etc. The desired ambient thermodynamic conditions can be realized in a constant-volume vessel [2] by applying a pre-burn approach or in a constant-pressure flow rig [3] using pre-conditioned gas mixtures. To create the most reliable experimental results, the Engine Combustion Network (ECN) [4] was established to collaboratively investigate combustion in representative engine conditions. The aim was to reduce the experimental uncertainties

* Corresponding author.
E-mail address: h.bao@tue.nl (H. Bao).

https://doi.org/10.1016/j.combustflame.2022.112610

in various experiments and between different set-ups [5]. As has been pointed out by Reitz [6], currently Computational Fluid Dynamics (CFD) is accurate enough to overcome limitations of experiments, but only when closely coordinated with experiments. Reynolds-averaged Navier-Stokes (RANS) is widely used in engine research due to its relatively affordable computational cost. A variety of excellent numerical studies regarding ECN cases within the RANS context have been carried out [7–10]. On the other hand, Large Eddy Simulation (LES) has been shown to be more suitable for modeling turbulent combustion due to its ability to reproduce transient large scale vortical and scalar structures [11]. An excellent review of atomization and spray combustion in a LES-framework was given by Jiang et al. [12]. More details about LES based approaches particularly concerning engine applications can be found in the review paper by Rutland [13].

Different combustion models have been used in LES, in combination with a variety of chemical mechanisms. The most straightforward of them is to directly express the filtered reaction rate in terms of the filtered thermodynamic variables (the homogeneous reactor model), neglecting the turbulence-chemistry interactions (TCI). Although possible important subgrid mixing effects are neglected in this "well-mixed" model, it was quite successful in predicting the ECN cases [14–16]. However, the high computational cost makes its application in LES a challenge. Alternatively, the flamelet concept [17], considering the turbulent combustion as an ensemble of local laminar flames (flamelets), drastically reduces the number of transport equations solved while detailed information is provided. Both *in-situ* [18] and tabulated flamelet models [19–21] have been successfully applied to the ECN cases and their capacity of predicting an igniting spray is extensively validated. The latter describe combustion with several independent controlling variables, generally chosen to be a mixture fraction Z and a reaction progress variable, and retrieves information from a prepared database.

Traditionally, the flamelet equations are derived using a transformation onto a local co-ordinate along the gradient of Z leading to a formulation defined in mixture fraction space [17]. For brevity, this flamelet approach is indicated by the classical flamelet model (CFM). The scalar dissipation rate (SDR) χ, which needs to be modeled in this case, appears as a flamelet parameter that characterizes the effect of local flow straining on the flamelet and directly determines the flamelet solution. A higher SDR corresponds to steeper scalar gradients and more rapid mixing. The flamelet database with SDR as parameter is used in the simulation of the more-dimensional (turbulent) system. Typically, the SDR is described by an analytical expression, e.g. an inverse error function of Z and proportional to the strain rate a of the stagnation-point at the oxidizer side of a laminar 1-D counterflow diffusion (CD) flame [17]. This analytic profile is function of mixture fraction and the applied strain rate: $\chi = \chi_{\text{Anal}}(Z, a)$. Even though this formulation of the SDR corresponds to a non-reacting stagnation flow, it is widely adopted in the igniting flamelet approach and gives good results with respect to ignition [18,22] and species formation [23]. The tabulated approaches applying this SDR model have been extensively applied to ECN cases [7,19,21,24–26].

FGM, on the other hand, is based on a set of flamelet governing equations derived from the full set of in-stationary three-dimensional conservation equations [27]. Unlike CFM, the flamelet equations, in this case, are solved in physical space and their derivation does not depend on whether the configuration is premixed or non-premixed. This set of strongly stretched flamelet equations (SSFE) depend on a mass burning rate, the arc-length perpendicular to the flame surfaces, acting as the eigenvalue of the system to characterize turbulent flow behavior. The change in mass burning rate can be included by stretch terms. All distortions from a local one-dimensional flame, including contributions due to stationary flow straining, curvature, density and velocity variations along the flame isocontours, are combined in a mass-based stretch rate K [28]. The leading idea of FGM is that the most important aspects of the dynamics inside the internal structure of the flame front should be taken into account [29]. Details regarding the related set of flamelet equations are briefly described in Section 2.1. Here, the stretch rate $K(x, \tau)$, as function of flamelet physical and time coordinates (represented by x and τ) respectively, follows from a transport equation that is derived from the momentum equation in transverse direction and depends on an imposed strain rate at the boundary of a counterflow configuration [27]. As the flamelet equations are solved in physical space, the SDR is not prescribed as function of Z like in CFM but is part of the solution. In fact, also the local value of Z is part of the solution. It is determined algebraically using Bilger's definition [30]. Consequently, in SSFE, SDR varies in time during ignition (indicated by $\chi = \chi_{\text{SSFE}}(Z, a, \tau)$, this is shown in Section 2.3.2) and is not a parameter that determines the flamelet solution. In a recent investigation, Sun et al. applied the SSFE SDR (physical solved solution) in a CFM solver when simulating igniting flamelets [31]. Although the SDR applied during ignition was approximated by only the inert mixing solution and assumed to be fixed in time ($\chi = \chi_{\text{SSFE}}(Z, a, \tau_0)$), still non-negligible differences were observed in temperature evolution compared to the solution based on $\chi = \chi_{\text{Anal}}(Z, a)$. It was found that an SSFE SDR is required for an accurate prediction of ignition, especially under more strained conditions, which is the case for engine-like sprays. Similarly, Göktolga et al. [32] addressed the limitation of applying the prescribed analytical SDR in a CFM solver when investigating the curvature effects. To apply the SSFE formulation in FGM, an explicit coupling of the local flow conditions to the applied strain rate in the flamelet is needed. An often adopted approach is to create a table that uses one specific strain rate which represents the influence of diffusion effects. The chosen strain rate needs to be justified by an additional argument in accordance with the intended application. Hence, for the basic FGM approach, the local strain rate or SDR is not used in the retrieval [33,34]. Notwithstanding that, both studies have shown that the basic FGM is a promising model in predicting the ignition of diesel-like spray. However, as is pointed out in the literature [21], the choice of the strain rate applied is somewhat arbitrary and the prediction of species information can be inaccurate while the IDT is well captured. The question arises whether better results can be obtained if the time-varying SDR obtained in an igniting SSFE calculation is used in the retrieval. The present work shows how this can be implemented and determines the improvements in predictions. The details of how the SDR can be added as an extra controlling variable are described in Section 2.3.

The following questions will be addressed in the case of solving the igniting flamelet in physical space: (1) What is the effect of the applied strain rate on an igniting flamelet? (2) How can the explicit $\chi_{\text{SSFE}}(Z, a, \tau)$ be included in the FGM as an extra controlling parameter? The proposed method is implemented in a newly developed solver in OpenFOAM [35] and validated with turbulent flame calculations. The expected benefit of the new approach is higher accuracy in ignition modeling and emission modeling. The strain rate effect on different stages of combustion within diesel-like spray has been studied earlier in a few investigations [36,37]. The influence of strain rate on soot evolution is different in the different soot formation stages (precursor formation, particle growth). The complex issue of soot prediction is still not solved yet [36] and also addressed in this work.

This study incorporates the SDR in the FGM method and evaluates its performance in predicting igniting spray via the ECN Spray A flame [38]. The paper is structured as follows: In Section 2, the construction and lookup algorithm of the extended FGM that includes the SDR effect is explained. The method is validated a pri-

ori on the laminar counterflow flame. Followed by an introduction to the spray modeling approach in Section 3, the LES framework set-up is presented in Section 4. After a validation of the turbulence modeling approach for the inert spray, the reacting simulations are presented where the extended FGM is applied. The detailed results are analyzed before a summary of conclusions is given in Section 5.

2. Flamelet analysis

2.1. Key ingredients of FGM

FGM can be applied to both laminar and turbulent flames. In both cases, transport equations for all controlling variables are solved together with the momentum and continuity equations. All other thermochemical properties, including temperature, can be directly retrieved from the tabulated manifolds according to the values of the local controlling variables [29].

2.1.1. SSFE

A representative laminar flame (flamelet) is needed for the tabulation, which is a CD flame for the case of diesel spray. In this way, the internal flame structure is decoupled from the computation of flow field. In the SSFE approach, employed here, the igniting flamelet equations are solved in physical space using detailed chemistry. The governing unsteady conservation equations of mass, species, and enthalpy within flamelet time coordinate τ read:

$$\frac{\partial \rho}{\partial \tau} + \frac{\partial \rho u}{\partial x} = -\rho K, \tag{1}$$

$$\frac{\partial \rho Y_k}{\partial \tau} + \frac{\partial \rho u Y_k}{\partial x} = \frac{\partial}{\partial x}\left(\frac{\lambda}{C_p}\frac{\partial Y_k}{\partial x}\right) + \dot{\omega}_k - \rho K Y_k, \tag{2}$$

$$\frac{\partial \rho h}{\partial \tau} + \frac{\partial \rho u h}{\partial x} = \frac{\partial}{\partial x}\left(\frac{\lambda}{C_p}\frac{\partial h}{\partial x}\right) - \rho K h. \tag{3}$$

Pressure is assumed a constant. In this work, preferential diffusion effects are ignored by the assumption of unity Lewis number. The local flame stretch rate $K = \frac{\partial v}{\partial y}$ is used to describe the change of mass flux perpendicular to the axis flow, the flame structure is thus disturbed by the "external" flow field via K [28]. Its conservation equation is given by:

$$\frac{\partial \rho K}{\partial \tau} + \frac{\partial \rho u K}{\partial x} = \frac{\partial}{\partial x}\left(\mu \frac{\partial K}{\partial x}\right) + \rho_{ox} a^2 - \rho K^2, \tag{4}$$

where ρ_{ox} and a are density and the prescribed strain rate in the oxidizer stream respectively. K is actually the local strain rate and locates the mass burning rate. It is a function of spatial coordinate x and time τ, and is highly dependent on the strain rate a applied. In fact, the specified strain rate ($a = -\frac{\partial u}{\partial x}|_{ox} = \frac{\partial v}{\partial y}|_{ox}$) is the boundary condition that is applied to Eq. (4), following the reference [39,40]. On the fuel boundary, $K_{fu} = a\sqrt{\rho_{ox}/\rho_{fu}}$. Discussion on this applied strain rate effect on ignition can be found in reference [41] and will be discussed in detail in Section 2.2. Its effect on species formation is also addressed Section 2.2. The equations are solved using the code CHEM1D [42]. The details regarding the mathematical modeling in CHEM1D can be found in [43].

2.1.2. Parameterization of the manifold

The Flamelet Generated Manifold approach [44] maps the considered set of SSFE flamelet solutions on a low-dimensional manifold by using a reduced number of controlling variables. The most important processes varying significantly in space and time in an igniting non-premixed flame are reaction and mixing. These phenomena can be appropriately included by a standard FGM parameterization using the mixture fraction Z and a progress variable Y_c. The mixture fraction is retrieved algebraically from the SSFE calculated mass fractions based on element conservation using weight factors as defined by Bilger. Y_c in general is a linear combination of a few representative species such that its value is monotonically increasing during the reaction progress from the unburnt mixing state until the chemical equilibrium. Then any thermochemical quantity can be tabulated as a function of Z and Y_c. The progress variable indicates the state of a reaction during ignition progress. For storage and retrieval at a certain mixture fraction, a normalized progress variable c_s is defined:

$$c_s = \frac{Y_c - Y_c^u(Z)}{Y_c^b(Z) - Y_c^u(Z)}, \tag{5}$$

where the superscripts u and b represent values obtained at a pure mixing and chemical equilibrium state, respectively.

It is the purpose of this study to consider SDR as an additional controlling variable in addition to progress variable. This is motivated by the sensitivity of ignition phenomena to strain rate. The relation between SDR and strain rate has been widely used in flamelet modeling. In the case of CFM approach, as mentioned, an analytic model expression for SDR $\chi_{Anal}(Z, a)$ is needed before the flamelet equations can be solved and a link between SDR values in turbulent flow and laminar flow is available. In the case of SSFE flamelets, however, SDR is part of the solution of the flamelet equations. For every time-dependent solution calculated with a fixed strain rate at the oxidizer boundary, a time-dependent spatial distribution of scalar dissipation rate χ is obtained from the solution as:

$$\chi_{SSFE} = 2D\left|\frac{\partial Z}{\partial x}\right|^2. \tag{6}$$

SDR is thus a function of Z, a, and τ. It is not a parameter that directly determines flamelet solutions. But, evolution of its values is indeed a consequence of the flamelet input a. For igniting FGM, typically only flamelet solution at a prescribed a is adopted according to the case studied. In order to consider SDR as an additional controlling variable that links the turbulence to different igniting flamelets, it is necessary to include information for a range of χ in the FGM table.

In the following subsections first the effect of strain rate on flamelets is demonstrated and next it is explored in detail which flamelets have to be taken into account in the FGM construction to represent the states in an igniting turbulent spray flame and how data from the FGM-table are retrieved in the application.

2.2. The effect of strain rate on flamelets

Here the sensitivity of ignition and soot precursor formation to strain rate in a counterflow configuration, corresponding to the ECN Spray A case of which a summary is given in Table 1, is analyzed. Detailed chemistry is modeled using the Yao et al. mechanism (54 species and 269 reactions) [45].

Full transient simulations of the CD-configuration with detailed chemistry will be compared to the transient simulations using FGM. Both are initialized by pure mixing and computed within CHEM1D. Here and in the following 'strain rate' refers to the boundary condition imposed at the oxidiser side of the counterflow equations in physical space (SSFE). The strain rate values cover a wide range from very low strain rate until the ignition limiting strain rate (a_{IL}, around 3250 s^{-1}). For each strain rate, the ignition delay time, denoted by IDT, is defined as the time when OH mass fraction for the first time reaches 2% of its maximum value following recommendation by ECN [4]. The flamelet solver only solves gas phase equations. To account for the heat-loss due to vaporization in the spray, the temperature at the fuel side of

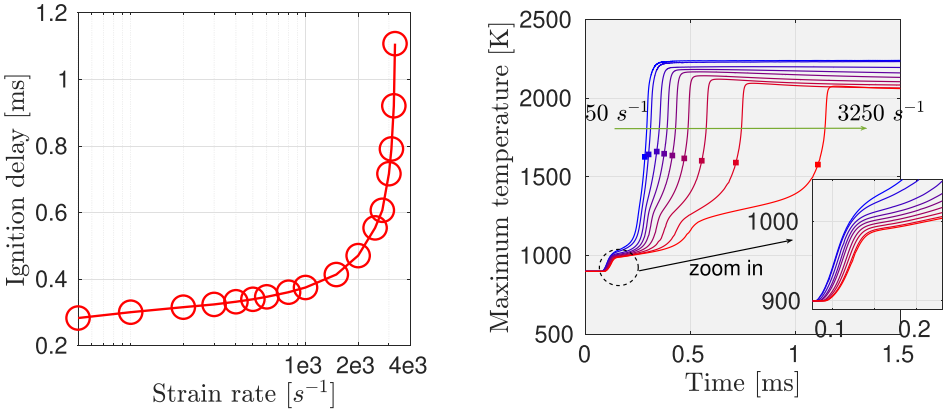

(a) IDT as a function of strain rate (logarithmic scale on the strain rate axis)

(b) Tendency of temperature rise on strain rate

Fig. 1. Effect of strain rate on ignition. The strain rate here and in the following figures refers to the applied strain rate at the boundary of the computational CD-configuration [39,40].

Table 1
Common specifications for ECN Spray A case.

Parameter	Specification
Injection conditions	
Fuel	n-dodecane
Nominal nozzle diameter	90 μm
Fuel temperature	363 K
Injection pressure	150 MPa
Ambient conditions	
Ambient temperature	900 K
Ambient pressure	6 MPa
Density	22.8 kg/m^3
Composition (molar)	reacting case: 15.00% O_2,75.15% N_2,6.22 %CO_2,3.62 %H_2O (stoichiometric mixture fraction 0.0456) inert case: 0.00% O_2,89.71% N_2,6.52 %CO_2,3.77 %H_2O

the flamelet is reduced to capture this effect as explained in reference [46]. To avoid the problem that thermal database is not defined for fuel temperature below 250 K, the fuel side boundary is set at a mixture fraction of $Z = 0.75$, i.e. a mixture of fuel and air. The states at $Z > 0.75$ are not encountered in the turbulent spray flame.

Figure 1 shows the effect of strain rate on ignition. As expected, it is seen in Fig. 1(a) that the IDT increases as the strain rate increases and finally approaches the so-called "ignition limiting strain rate". Reports on previous investigations [33,34] declared that the IDT is insensitive to the strain rate when it is smaller than 1000 s^{-1}, however, this is highly dependent on the chemistry mechanism applied. For the Yao mechanism, the difference is significantly higher than that for the Stanford mechanism analyzed in reference [34]. Fig. 1(b) shows the temperature rise tendency during an ignition with various strain rates. The curves from left to right indicate the strain rate value of 50, 100, 500, 1000, 1500, 2000, 2500, 3000, 3250 s^{-1}. The square markers indicate the 2% OH-based IDTs for each strain rate. The later stage of ignition is indeed more sensitive to strain rate compared to the first-stage ignition.

A detailed analysis of the ignition can be found in Fig. 2. For all strain rates, it is seen that the ignition starts at lean mixtures due to the higher initial temperature and propagates to rich mixtures in the first stage of ignition. During the second stage, the peak temperature location returns to Z_{st}. The shift of the peak temperature location into the rich zone depends on the strain rate. The ignition propagates towards the richer mixture since the diffusion of energy and species changes the chemical activity. The diffusion stage is also influenced by the strain rate. More details can be found in literature [36] and [47].

As is mentioned in Section 1, next to ignition behavior, also, soot formation is influenced by strain rate. The phenomena occurring during the transition of gaseous soot precursors to solid soot particles has been studied extensively, and an excellent summary can be found in reference [48]. In soot formation modeling, most often acetylene (C_2H_2) is taken as the soot precursor as it is a most relevant species for soot growth. As can be seen clearly in Fig. 3, the formation of C_2H_2 in a CD flame is highly dependent on the strain rate. The mass fraction of C_2H_2 is very low during the first stage of combustion. A significant rise is only seen during high temperature reactions. The peak of C_2H_2 appears in the richer mixtures and moves towards the fuel side during ignition. Note that even when the combustion reaches steady-state in terms of temperature, C_2H_2 keeps evolving and spreading to the richer side until it finally approaches equilibrium. The trend is more prominent as the strain rate increases. As the commonly progress variable definitions are mostly proposed to capture ignition, only intermediate species during the ignition are taken into account. This was found to give a problem in capturing C_2H_2 accurately. Thus, to solve this here a new reaction progress variable is introduced. It is defined as follows:

$$Y_c = 1.5Y_{CH_2O} + 2.7Y_{HO_2} + 1.2Y_{H_2O} + 1.2Y_{CO_2} + 0.9Y_{CO} + 2.5Y_{C_2H_2}. \quad (7)$$

The first 5 species and their weighting factors in this new Y_c definition follow from a previous study [46], in which this combination was extensively validated. The addition of C_2H_2 is due to the aforementioned fact that an ignition-based Y_c definition does not capture the evolution of minor species that are responsible for soot production. In order to include the identification of reaction progress towards for soot, C_2H_2 is included. The weighting factor is carefully chosen by ensuring the new Y_c definition meets the following criterion: (1) Each value of Y_c must correspond to a unique state of reaction, so that Y_c monotonically increases as function of time. (2) Y_c has to reveal the temporal evaluation of C_2H_2 in mixture fraction space.

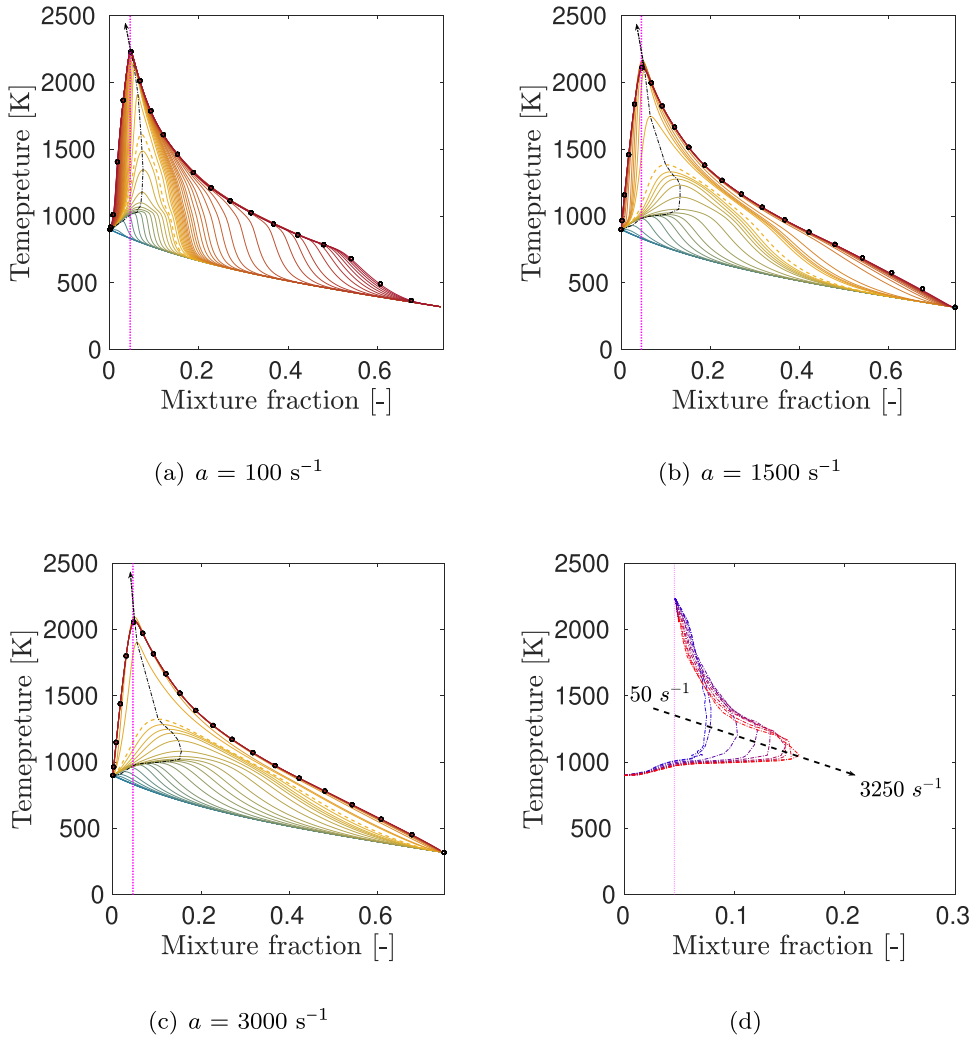

Fig. 2. Influence of strain rate on ignition. The vertical dotted lines are the stoichiometric mixture fraction. For (a)(b)(c), solid lines are the unsteady flamelets, the flamelets at the IDT are represented by dashed lines, the dashed-dotted lines ending in arrow indicate the maximum temperature, while the steady-state flamelets are marked by circles (○). Top: 100 s^{-1} strain rate (left), 1500 s^{-1} strain rate (right), bottom: 3000 s^{-1} strain rate (left), change of maximum temperature during ignition for different strain rates (right).

The performance of the newly defined Y_c in capturing both the temperature and acetylene is evaluated by contour plots for a case with strain rate 500 s^{-1} shown in Fig. 4. The results for the previous Y_c is also shown for comparison. The contour plots are colored by mixture fraction. Although both Y_c definitions perform well for temperature (for a specific color, i.e. a specific mixture fraction, temperature follows the Y_c well), the performance of capturing the $Y_{C_2H_2}$ show differences. In the case of the previous Y_c definition, the evolution $Y_{C_2H_2}$ is badly resolved in the later stage of reaction for all the mixture fractions. To be precise, for $c \to c_{end}$, $\frac{\partial Y_{C_2H_2}}{\partial c} \sim \infty$. This results in the fact that small interpolation errors can have a large effect on the value for $Y_{C_2H_2}$. The performance of this new Y_c definition has also been tested for the Narayanaswamy mechanism (257 species and 1521 reactions). A good agreement with the detailed chemistry results is observed. This is shown in Appendix A.

The necessity of including the effect of applied strain rate in CHEM1D can be seen more clearly via the new Y_c definition. Contour plots of source of Y_c and mass fraction of C_2H_2 are shown in Fig. 5. For all strain rates, three regions with higher values of Y_c source are observed. However, the magnitude and distribution of source vary with strain rate. This implies that the evolution of Y_c is different for each strain rate. Also, the peak of Y_c shifts to $Z = 0.1$, which is different from Z_{st} observed for the previous Y_c definition (not shown here for brevity). This is due to the presence of acetylene in the new Y_c definition, which typically occurs at rich conditions.

To conclude, the strain rate effect cannot be ignored for both ignition and soot formation. An extension of the FGM method to include strain rate variations is thus needed.

2.3. Extended FGM including strain rate variation

In order to open the discussion in this section, the plot of peak temperature of steady CD flames as function of the applied constant strain rate, known as the “S-curve”, is first introduced. Fig. 6 represents an S-curve for the standard ECN Spray A condition [4] based on computed CD flames. The peak temperatures of burning flamelets lie along the curve $b - d - f$. Peak temperature of non-burning flamelets lie along the curve $i - g$. The end point f corresponds to the extinction strain rate for a series of steady flame with increasing strain rate. The end point g corresponds to the ignition limiting strain rate a_{IL}, beyond which the flamelet will not auto-ignite towards the upper branch $d - f$. More states can be reached by unsteady solutions. At fixed strain rate lower than a_{IL}, flamelets will auto-ignite and evolve towards the steady burning

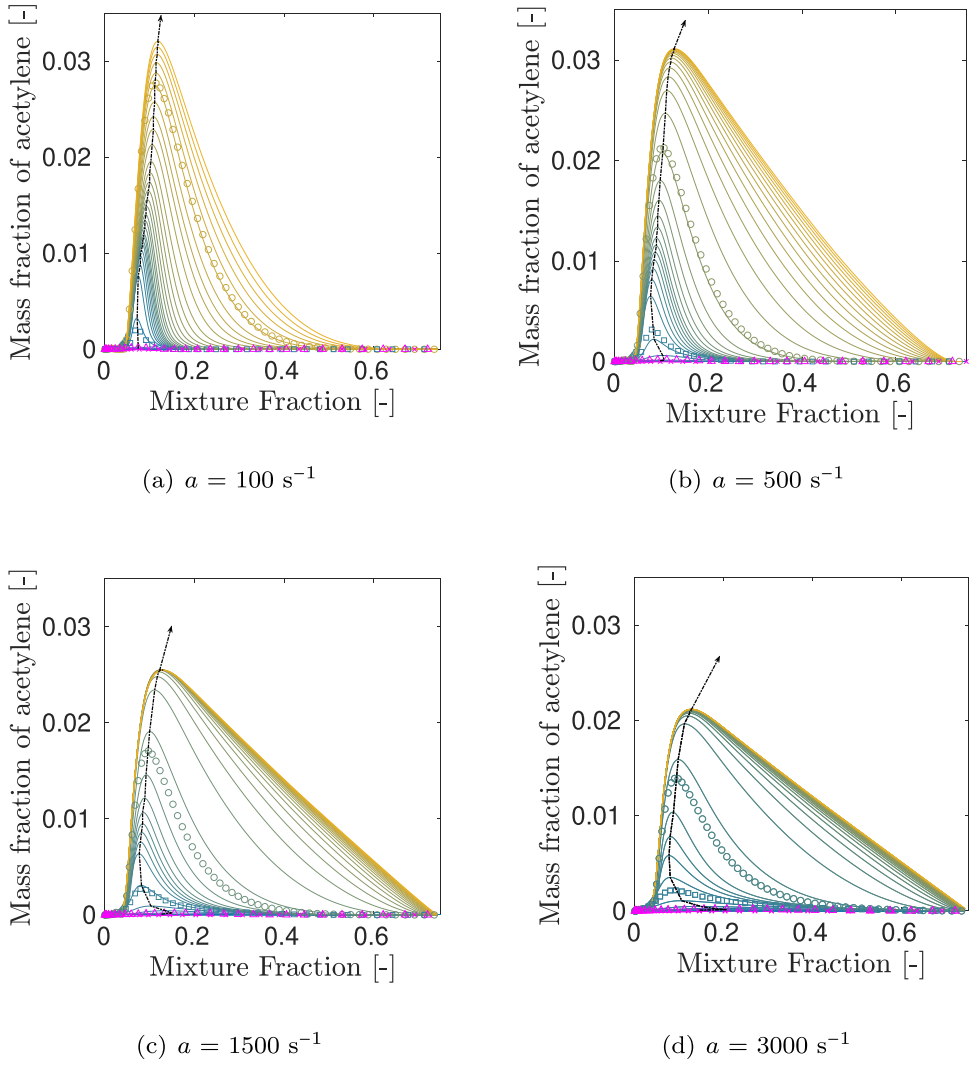

Fig. 3. Influence of strain rate on acetylene. Solid lines are the distributions of acetylene during the ignition progress, the dashed-dotted line ending in arrow indicates the development in time. The acetylene distribution at IDT_1 and IDT_2 are marked by x-marks (x) and triangles (△), respectively. Squares (□) mark the distribution at IDT. The steady-state for temperature starts is marked by circles (○). Top: 100 s^{-1} strain rate (left), 500 s^{-1} strain rate (right), bottom: 1000 s^{-1} strain rate (left), 3000 s^{-1} strain rate (right).

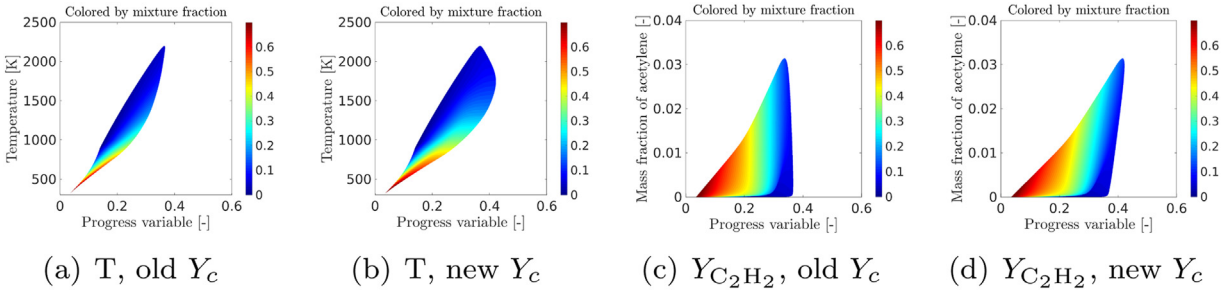

Fig. 4. Performance of the progress variable on temperature and mass fraction of acetylene.

states $b-d$. This set of states will be called 'Region I'. Between the strain rate for extinction and ignition, an unstable solution branch exists. It separates regions that evolve to either the upper or the lower stable branch. This set of states will be called 'Region III'. Flamelet solutions with time varying strain rate can show more complex behavior. A rapid increase of strain rate can bring the system in the region where the temperature is higher than what could be maintained at the new strain rate. This set of states will be called 'Region II'. In the context of the CD-configurations, such situations can be explicitly calculated. But, it would lead too far to include the many possible histories in an FGM. Instead, a simplified description of the extension of the manifold to region II is needed.

We now give a more detailed description of the different possible types of unsteady evolutions in the three regions of Fig. 6:

(I) **Region I** ($a-b-d-g-j-a$) This region contains the igniting flamelets for a wide range of strain rates below a_{IL}.

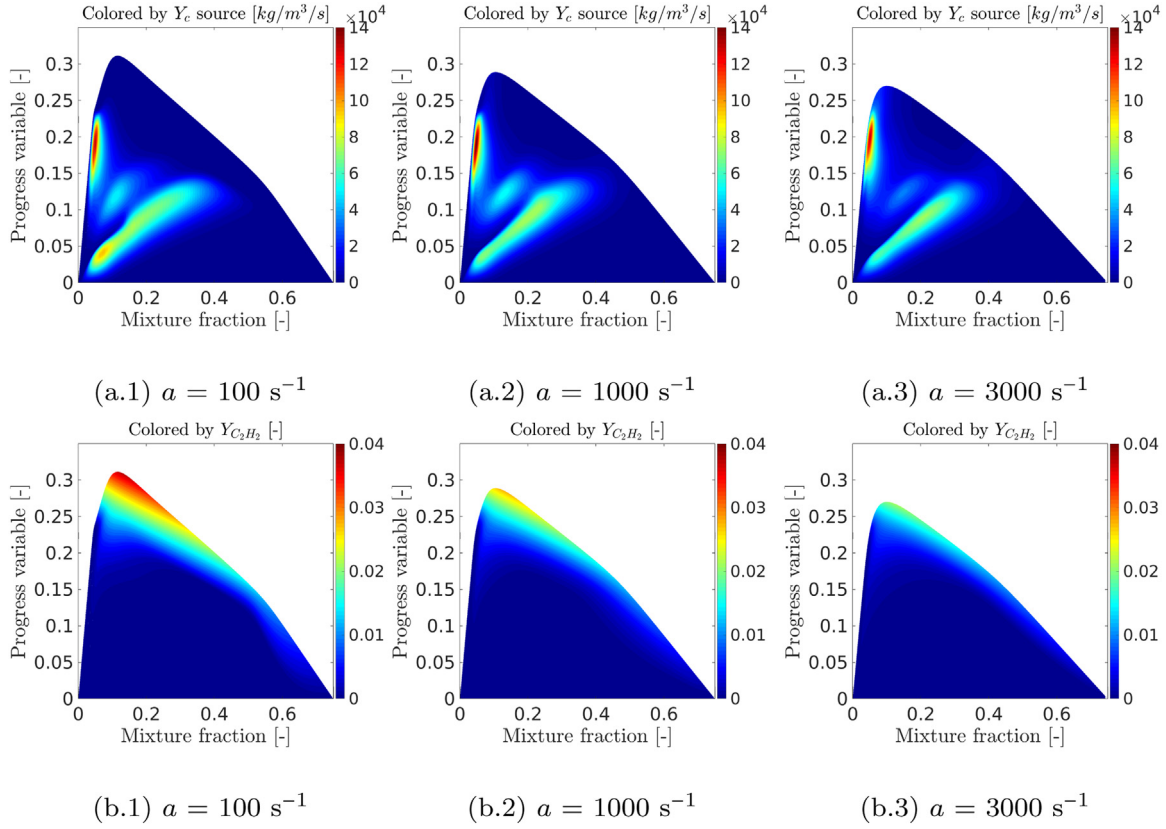

Fig. 5. Contour plots of source Y_c (top) and mass fraction of C_2H_2 (bottom) in progress variable and mixture fraction space for different strain rates.

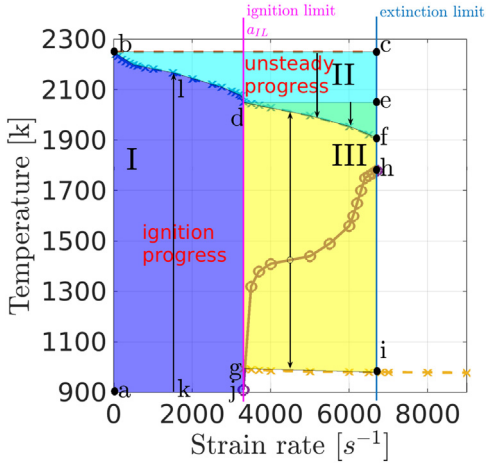

Fig. 6. Peak flamelet temperature versus strain rate. The S-shaped curve.

The arrow in this region refers to the ignition progress at a representative strain rate from the pure mixing state to the equilibrium, which is adopted for tabulation by typical igniting FGM.

(II) **Region II** $(b-c-e-f-d-b)$ This region can be accessed during unsteady response to a change of strain rate. When the strain rate variation is slow or stops, an unsteady evolution will bring the flamelet to a steady flamelet state at the lower boundary of region II.

(III) **Region III** $(d-f-h-i-g-d)$ This region is bounded by non-burning $(g-i)$ and burning $(d-f)$ steady flamelet states and contains the unstable branch $g-h$. Note that auto-ignition starting from the initial mixing condition at a strain rate higher than a_{IL} stabilize at $g-i$, which is seen as non-burning considering its low temperature.

More details regarding the three regions can be found in Section 2.4. In the following part, FGM will be extended to include all the three regions rather than depending on a single representative igniting flamelet in region I. This extension is denoted by "multi-strain-rate FGM" (mFGM) in this study. For tabulation, a full set of igniting flamelets at different strain rates, ranging from 50 s^{-1} until a_{IL}, are used (see Section 2.3). The performance of applying this tabulated database to different regions is evaluated in Section 2.4. First, the details regarding the tabulation and retrieval algorithm of the mFGM method are discussed.

2.3.1. Tabulation of mFGM database: normalization of progress variable

A key step in the practical use of an FGM is the relation between non-normalized and normalized progress variable (Y_c and c_s, respectively). The range of Y_c depends on its definition and on the value of other controlling variables (mixture fraction and in this case strain rate a). For the standard FGM method this is expressed by Eq. (5). However, when a is introduced as an extra controlling parameter, also the range of the reaction progress variable depends on the applied strain rate and the notations $Y^u_{c|a}(Z)$, $Y^b_{c|a}(Z)$ and $c_{s|a}(Z)$ can be used to represent this. In unsteady and highly turbulent diesel-like sprays, as a consequence of rapid SDR variations local values of the progress variable may be higher than the value $Y^b_{c|a}(Z)$ deduced from a flamelet evolving at a fixed strain rate. In order to accommodate this, the tabulated range of Y_c at a certain strain rate value must contain not only states in region I, but also states in region II such that the full range of Y_c occurring in the spray flame is contained in the table. For this purpose here the

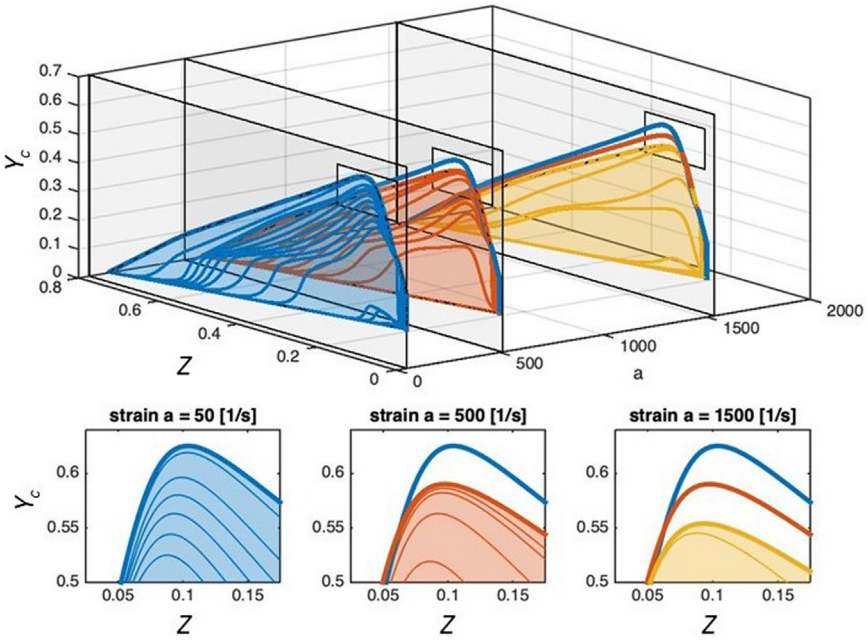

Fig. 7. A virtual mFGM with 3 manifolds (a=50, 500 and 1500 s^{-1}). Solid colored surfaces represent the igniting flamelet regime (with several instances of each igniting flamelet shown for reference). The additional figures give a zoom (see small box in top figure) of each individual FGM with the added flamelets.

normalized progress variable at certain Z and a is defined as:

$$c_{s|a}(Z) = \frac{Y_c - Y^u_{c|a}(Z)}{Y^{max}_c(Z) - Y^u_{c|a}(Z)}. \tag{8}$$

In this expression $Y^{max}_c(Z)$ is the maximum among all $Y_{c|a}(Z)$. Consequently, for an igniting flame evolving at a constant Z and a, its final state corresponds to a normalized progress variable value (in general) lower than one, say $c^{max}_{s,ig|a}(Z)$. The states, $c_{s|a}(Z) \in [c^{max}_{s,ig|a}(Z), 1]$, are the added flamelet states in Fig. 7, which belong to region II. In other words, for a =500 s^{-1}, $c_{s|500}(Z)$ is extended to 1 by adding the flamelet solutions corresponding to $c_{s|50}(Z) > c^{max}_{s,ig|500}(Z)$. Now the data of the computed unsteady flamelets can be tabulated on a regular mesh in parameter space $(Z, c_{s|a}(Z), a)$. The mesh has 301 points for Z, 501 for c_s and 17 for a. In the Z direction, a clustering around the stoichiometric value is used.

2.3.2. Dynamics of scalar dissipation rate in igniting flamelets

In mFGM, the thermochemical properties are stored in the database as function of the controlling variables $f(Z, c_{s|a}(Z), a)$. In a more-dimensional (turbulent) situation, the strain rate cannot be retrieved simply from the velocity field. In fact one would have to derive a local relative velocity field taking into account the velocity of the flamesheet itself. Thus, it is preferable to use the scalar dissipation rate. The questions arise: what is the relation between scalar dissipation rate and strain rate in a flamelet? In CFM, the correlation relies on an approximate analytical expression which is derived for a steady counterflow flamelet (see [17], Eq. (2.38)). It provides χ as function of a at each value of Z ($\chi_{Anal}(Z, a)$). Alternatively, as is described in Section 2.1, the distribution of scalar dissipation χ in SSFE can be calculated explicitly (Eq. (6), leading to $\chi_{SSFE}(Z, a, \tau)$ as a consequence of the time-dependent Z in a physical 1-D CD flame. These two procedures are used in the approaches called Case 2 and Case 3, respectively, in Sections 4.2.1–4.3.

To obtain a unique solution, it is a requirement that χ is related uniquely to a at each pair of values of Z and c. Hence, χ must be a monotonous function of a for any given Z and $c_s(Z)$. In the case of $\chi_{Anal}(Z, a)$, χ is a monotonous function of a and independent of c. The difference between χ_{Anal} and χ_{SSFE} is shown in Fig. 8. Figure 8(a) takes a = 500 s^{-1} as an example. During ignition, χ_{SSFE} varies with time, its peak moves towards the richer mixture in the beginning and moves back in the end. The steady-state χ given by SSFE is different from the analytical expression which also relies on an additional assumption on the density profile. Fig. 8(b) shows the values provided by the two methods in a wide strain rate range. It is observed that the steady-state χ_{SSFE} is more skewed towards the stoichiometric mixture fraction than χ_{Anal}. It is clear that a significant difference between peak values exists. Thus, it can be expected that χ_{Anal} is not a good choice to identify the strain rate as a function of time (or Y_c). Recently, this was also addressed for igniting hydrogen flames [31].

2.3.3. Implications for an mFGM database construction and use

To utilize the SDR as parameter to link conditions in a computed flame to states in the mFGM, it is essential to check whether it is possible to identify a unique strain rate a for a scalar dissipation rate χ_{SSFE} at every Z and c_s. Figure 9 shows results for several representative mixture fractions. The relation between χ_{SSFE} and a is evaluated for different $c_s(Z)$ levels. Only the states that $c_{s|a}(Z) \le c^{max}_{s|a}(Z)$ are shown (igniting flamelets, region I). It is seen that χ for all $c_s(Z)$ and Z monotonically increases with a such that a can be uniquely identified by specifying χ. The correlation is linear at pure mixing (small c_s value) whereas a non-linear correlation is seen as the flame develops ($c_s > 0.1$). The Fig. 9 shows that for given Z, χ, and c_s, value of the strain rate parameter can be identified. However, it can also be seen that for some values of Y_c and Z at high values of χ, there is no corresponding flamelet condition as expected. The limiting value of scalar dissipation rate is denoted by $\chi^{max}_{|c_s}(Z)$.

When mFGM is extended to states above the steady-state flamelets (region II) by copying flamelet states from steady solutions at lower strain rates (a general procedure for FGM table generation [34]), the monotonous relation is lost. Increasing trend of scalar dissipation rate with strain rate is only present in the igniting flamelet regime. E.g. as seen in Fig. 7, the extensions of the igniting flamelets at both 500 and 1000 s^{-1} use data from the steady flamelet at 50 s^{-1}. Their added flamelets have the same χ.

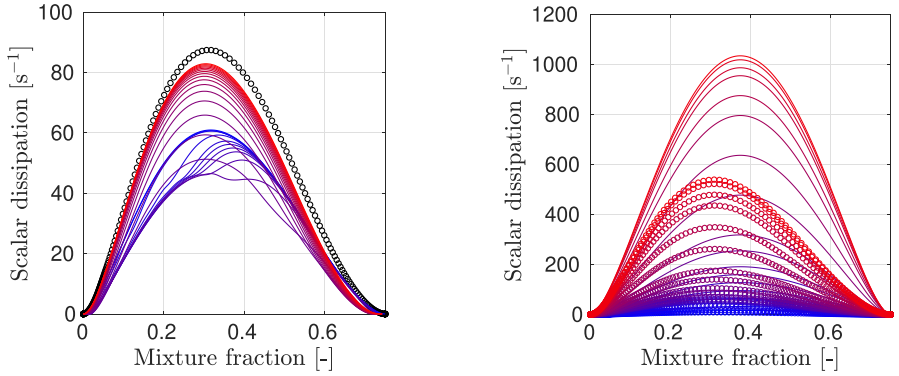

(a) Scalar dissipation rate evolution in SSFE, $a = 500\ \mathrm{s}^{-1}$. Blue to red: the reaction progress from pure mixing until the equilibrium. The distribution of steady-state is marked by circles (∘).

(b) The steady-state scalar dissipation by SSFE (marked by circles (∘)) and the scalar dissipation given by the analytical expression (solid lines). Blue to red: $a = 10\ \mathrm{s}^{-1}$ to $a = 3250\ \mathrm{s}^{-1}$.

Fig. 8. Difference between the scalar dissipation rate in numerically computed flamelets and the analytical model for steady flamelets.

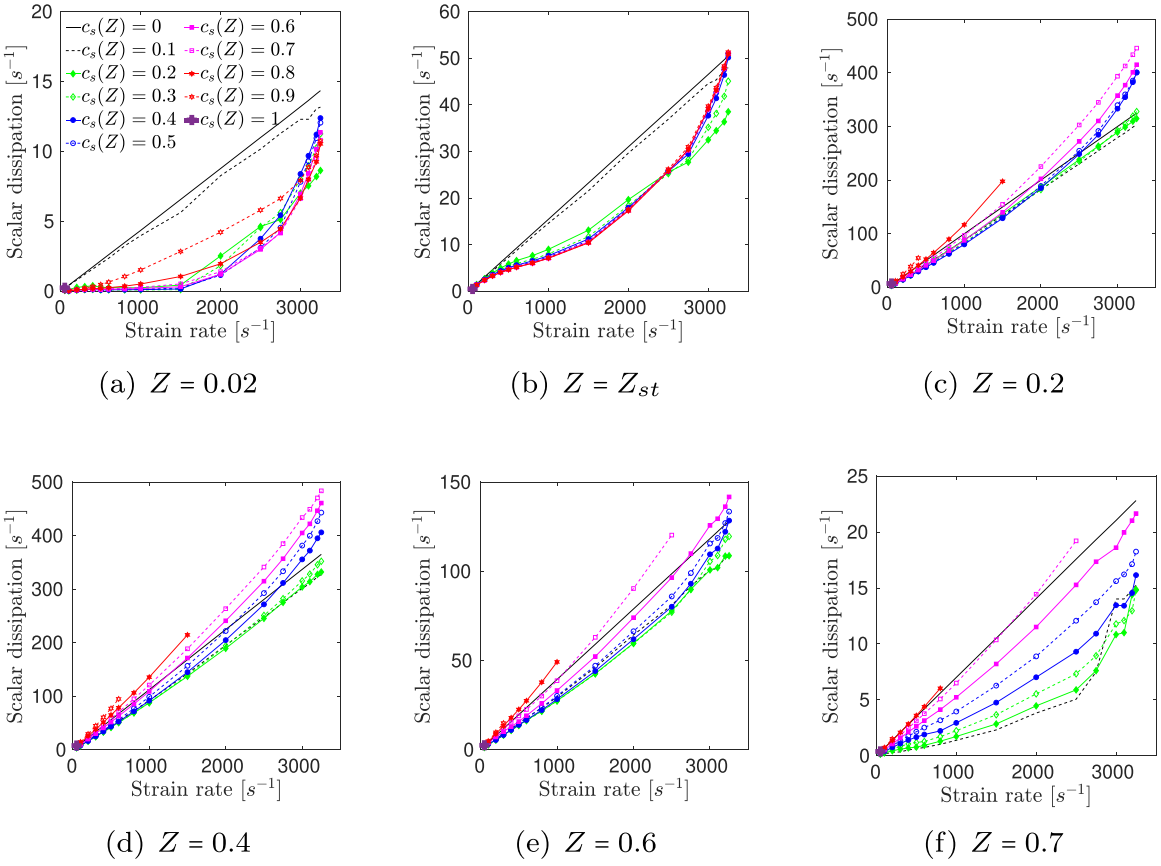

Fig. 9. Dependency of scalar dissipation on strain rate according to representative mixture fraction. Different symbols indicates different value of scaled progress variable. The strain rate here refers to the applied strain rate in CHEM1D.

In Fig. 10 values of χ are displayed as function of the corresponding strain rate for several combinations of mixture fraction and scaled progress variable. For high value of χ it does occur that there is no corresponding a. This can be illustrated by the following example concerning states at the stoichiometric mixture fraction for two values of scaled progress variable $c_s(Z_{st}) = 0.96$ and $c_s(Z_{st}) = 0.98$. In the first case all values of SDR needed are immediately available at corresponding strain rate (the dashed-dotted line). In the second case there is an SDR beyond which a corresponding strain rate is not available. The limit SDR corresponds to the a limit strain rate value a_{lim} (the dotted line). A flamelet state corresponding to this situation can be defined by assigning a virtual SDR value to high strain rate states using a linear extrapolation line starting at the limit state. This is done such that

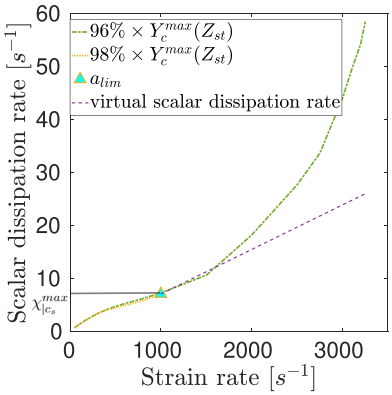

Fig. 10. Scalar dissipation tendency on strain rate at Z_{st} at different Y_c. The strain rate here refers to the applied strain rate in CHEM1D. a_{lim} refers to the strain rate up to which igniting flamelet exists.

the monotonically increasing trend of strain rate with scalar dissipation rate is maintained. For every strain rate the corresponding value of SDR on the extrapolation line is stored in the mFGM lookup table (Fig. 10). Then in two steps local properties can be retrieved from the table: the high SDR is mapped onto a strain rate via the virtual correspondence and next the equilibrium data for an igniting flamelet with the same value of normalized progress variable is used. This procedure is insensitive to the slope of the proposed virtual correspondence line, because independent of the (positive) slope it leads to the same state at lower a.

2.3.4. Illustration of trends with strain rate

Fig. 11 illustrates the variations of several properties as function of the applied strain rate at the stoichiometric mixture fraction as an example. These plots clearly illustrate that the soot precursor, acetylene, is significantly changed by a. However, the temperature at fixed c_s is barely influenced by a. The difference mainly exists when approaching the steady-state, as observed in Fig. 6. This is why for IDT and LOL, a FGM based on a single strain rate

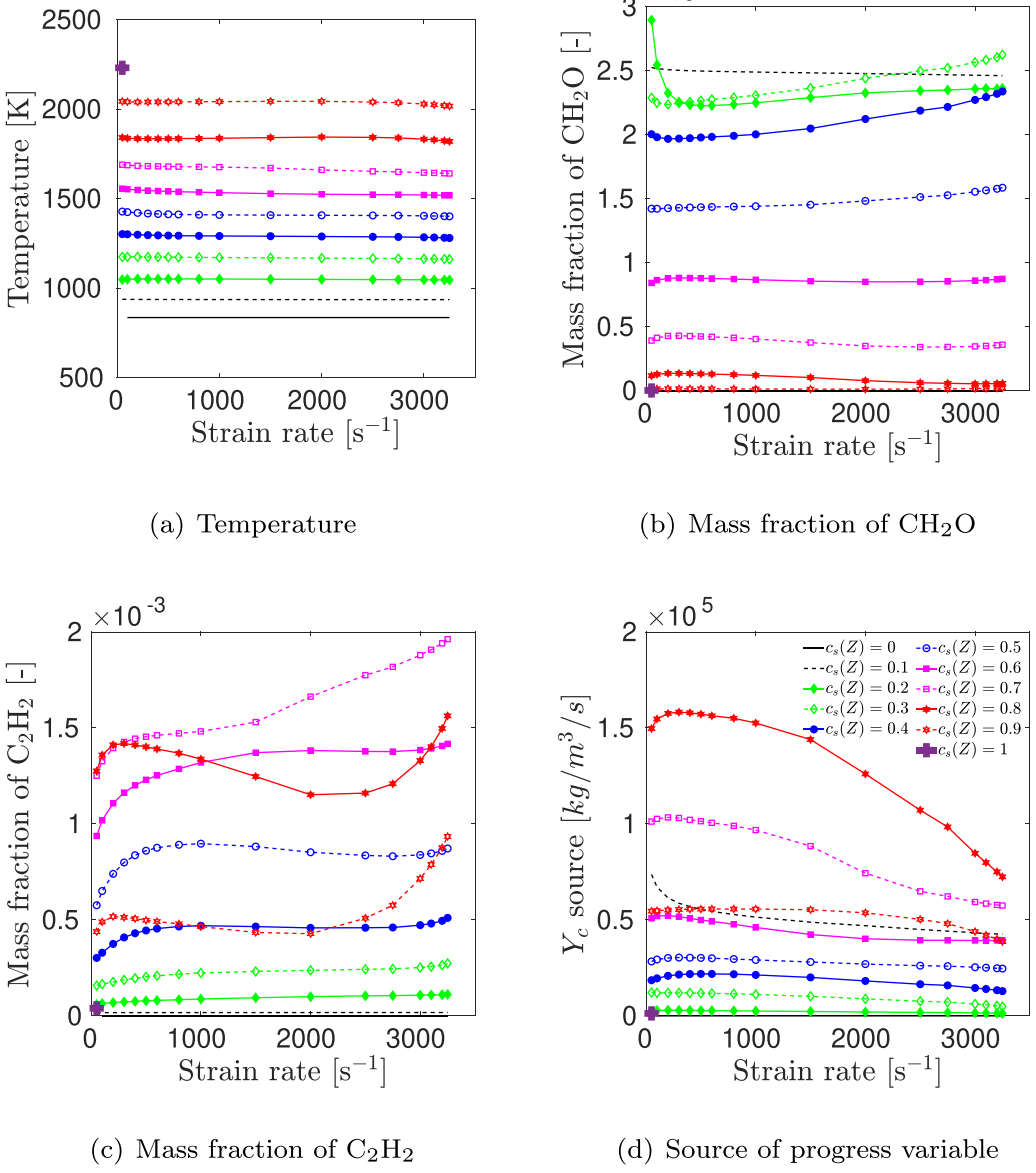

(a) Temperature

(b) Mass fraction of CH_2O

(c) Mass fraction of C_2H_2

(d) Source of progress variable

Fig. 11. Change of retrieved properties with strain rate at stoichiometric mixture fraction Z_{st} and different normalized progress variable c_s. The strain rate here refers to the applied strain rate in CHEM1D. Different symbols indicates different values of normalized progress variable.

is acceptable. However, species information shows difference. The source term of progress variable is significantly affected by a as the new progress variable definition takes the acetylene into account. As some properties are not changing linearly with a, the interpolation in strain rate direction is chosen to be done by a piece-wise cubic interpolation [49] in between the selected strain rates.

2.3.5. Lookup algorithm of the extended mFGM

Now the procedure to link flame properties to controlling variables can be fully specified. Flame states are attributed to the regions I, II and III in Fig. 6, depending on values of scalar dissipation rate and progress variable (We recall temperature in Fig. 6 can be replaced by progress variable). The main subdivisions between different cases can be described as follows. For a flame condition characterized by Z, Y_c, χ, a corresponding normalized progress variable c_s is first identified according to Eq. (). If $\chi > \chi^{max}(Z, c_s)$ and $c_s < c^{max}_{s,ig|a_{IL}}(Z)$, the flame state lies in region III and the properties are those of the flamelet at the ignition limit strain rate. If $\chi \leq \chi^{max}(Z, c_s)$, a strain rate value corresponding to χ can be found and depending on the value of the normalized progress variable, the flame state lies in either region I or region II. The final possibility is that $\chi > \chi^{max}(Z, c_s)$ and $c_s > c^{max}_{s|a_{IL}}(Z)$. This also falls in the region II. In all cases, the dependent flame properties are retrieved by interpolation on the mesh of the mFGM database with independent variables Z, c, a.

2.4. A priori validation: performance of the mFGM database

It must be proven first in the laminar framework that FGM captures the flame develpoment before it can be applied in turbulent application. In this section, the performance of the mFGM is presented for the three regions defined in Fig. 6. For each region, counterflow laminar flame at a certain strain rate chosen using FGM is computed with the mFGM database and compared to the corresponding detailed simulation. All three regions are presented. In FGM approach, only transport equations for controlling variables are solved. Here, computation with mFGM means that transport equations are solved for the controlling variables Z and Y_c, and all dependent properties are retrieved from the mFGM table according to Z, Y_c, and a. In the context of laminar flames, transportation of controlling variables Z and Y_c follows:

$$\frac{\partial \rho Z}{\partial \tau} + \frac{\partial \rho u Z}{\partial x} = \frac{\partial}{\partial x}\left(\frac{\lambda}{C_p}\frac{\partial Z}{\partial x}\right) - \rho K Z. \tag{9}$$

$$\frac{\partial \rho Y_c}{\partial \tau} + \frac{\partial \rho u Y_c}{\partial x} = \frac{\partial}{\partial x}\left(\frac{\lambda}{C_p}\frac{\partial Y_c}{\partial x}\right) + \dot{\omega}_{Y_c} - \rho K Y_c. \tag{10}$$

It is noted that the source term $\dot{\omega}_{Y_c}$ is directly retrieved from the pre-tabulated database. As is already mentioned, species mass fractions and other thermochemical properties are generally retrieved directly from the manifold. But, for species that are varying slowly, it is better to solve a transport equation following Eq. (2) and retrieve the corresponding source term $\bar{\dot{\omega}}_k$ from the table [44]. The two schemes are referred to as “direct retrieval” and “transport”, respectively. It is noted that the latter also applies information from the FGM database. The latter applies to certain species depending on the application. In this work, it will be applied for C_2H_2.

2.4.1. Region I

The test flame is any igniting flamelet in Region I. Agreement on IDT and C_2H_2 are used for validation. In Fig. 12, the IDT predicted by mFGM and standard FGM that is based on the igniting flamelet at $a = 500$ s^{-1} (FGM_{500} for brevity), respectively, are presented for a wide range of strain rates. It is seen that the mFGM always is in good agreement to the detailed chemistry results. The FGM_{500} only provides an accurate IDT around the prescribed strain rate value. It also over-predicts the ignition limiting strain rate considerably, whereas the mFGM captures it well. Note that this is especially the case for the Yao mechanism applied here. The sensitivity of IDT on strain rate is higher than that is found for the Narayaswamy mechanism. The latter actually shows a relatively small dependency on the strain rate for strainrates below 1000 s^{-1} [34].)

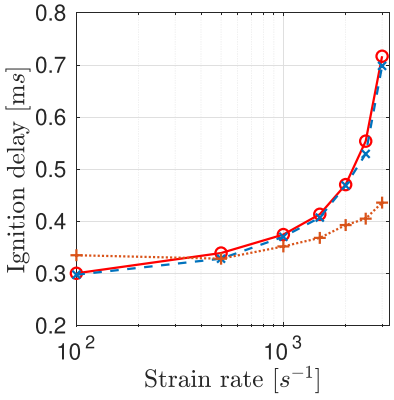

Fig. 12. Comparison of IDT predicted by mFGM(x), single-stran-rate FGM at a =500 s^{-1}(+), and detailed chemistry(○).

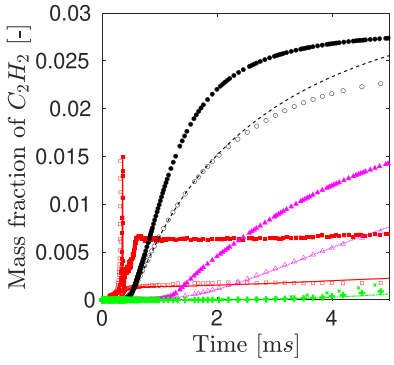

Fig. 13. Development of C_2H_2 for a case with $a = 150s^{-1}$ at mixture fractions $Z = Z_{st}$ (red), 0.2 (black), 0.4 (magenta), and 0.6 (green). Detailed simulations (lines), mFGM (open symbols) and FGM_{500} (solid symbols) are shown. For visualization, the mass fraction at Z_{st} is multiplied by 10. The legend is also shown in Table 2.

Table 2
Legend of Fig. 13.

	$Z = Z_{st}$	$Z = 0.2$	$Z = 0.4$	$Z = 0.6$
Detailed	———	- - -	·····	-·-·-
mFGM	□	○	△	+
FGM_{500}	■	●	▲	x

Figure 13 shows the prediction of C_2H_2 development given by mFGM and FGM_{500} at $a = 150$ s^{-1} as an example. For mFGM, interpolated values at $a = 150$ s^{-1} using a piece-wise cubic interpolation are applied (see also 2.3.2). The figure illustrates that for an igniting flamelet at a certain strain rate, mFGM captures the acetylene well. The typical FGM using a single strain rate (FGM_{500}) over-predicts the acetylene levels significantly.

2.4.2. Region II

Regarding the unsteady flamelets above $b - d - f$, the added equilibrium solutions at lower strain rates are used. The performance of mFGM is shown in Fig. 14. The steady flamelet created at strain rate 50 s^{-1} is used to initialize a transient simulation with

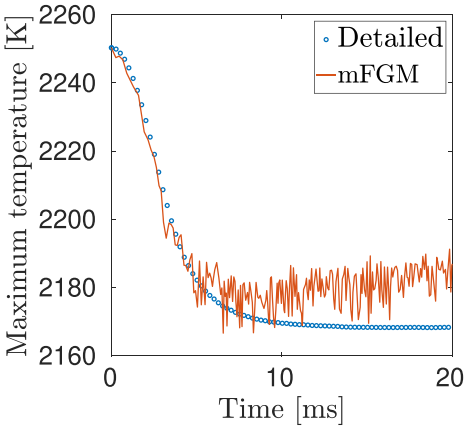

(a) Temperature

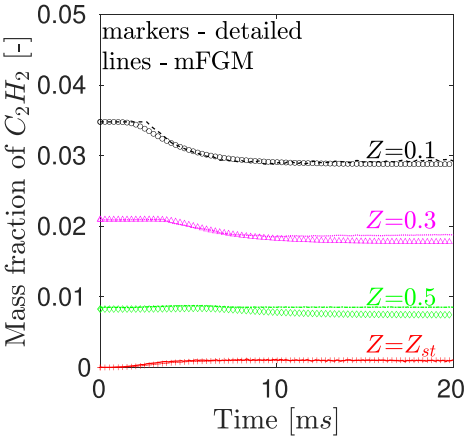

(b) Change of mass fraction of C_2H_2 with time at representative mixture fraction

Fig. 14. The unsteady flame development from the equilibrium at a =10 s^{-1} to a =500 s^{-1}, detailed and mFGM. Infinitely time step in the change of strain rate.

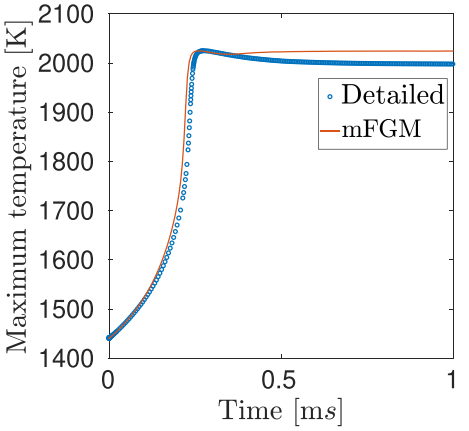

(a) Temperature

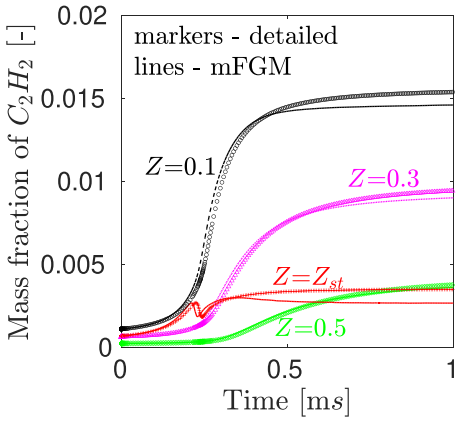

(b) Change of mass fraction of C_2H_2 with time at representative mixture fraction

Fig. 15. The progress from the unsteady branch at a =5000 s^{-1}, detailed and mFGM. The igniting case.

an applied strain rate of 500 s^{-1}. The predicted development of the unsteady flame given by mFGM is compared to the simulation that applies the detailed chemistry. Although temperature oscillations are seen in the quasi-steady period (which is an interpolation issue at the maximal progress variable), the trend is captured reasonably well. As the unsteady progress to the equilibrium state is slow compared to the ignition progress, and the temperature fluctuation is very small compared to its magnitude, the mismatch is acceptable. The evolution of acetylene is well-captured over the complete mixture fraction range.

2.4.3. Region III

Although **Region III** is introduced as the yellow region in the S-shaped curve, the whole region $d-e-f-h-i-g-d$ (i.e. every state above the ignition limit) is treated together. For all of these states, a single entry, of the igniting flamelet with highest strain rate, is used. In other word, information at the boundary of the mFGM (the highest available strain rate in the table) is applied for **Region III**. To test this approach, a state that does and one that does not ignite at a =5000 s^{-1} (slightly above and below the unsteady branch $g-h$, respectively) are studied (Figs. 15 and 16). The temperature and acetylene are captured perfectly in both cases by the FGM approach. Only a slight mismatch is seen between mFGM and detailed chemistry when approaching the steady-state. This was also pointed out by Wehrfritz et al. [34] and is due to the fact that the progress variable value of an unsteady flamelet slightly overshoots before it relaxes to its equilibrium value. This part of the unsteady flamelet solution is generally discarded in the FGM approach to ensure the monotonicity of the progress variable.

From this priori analysis, it can be concluded that the mFGM captures both the ignition delay and the evolution of acetylene accurately as function of the strain rate. In the next section, the approach will be applied in an LES study of the ECN spray A flame.But first we elaborate the special treatment of acetylene.

2.5. Acetylene formation modeling

In Section 2.2 we have defined a progress variable leading to better description of C_2H_2. This is sufficient for accurate tabulation of both value and source term of Eq. (2) in the CD flame. In the soot formation model used in the current investigation (described in Section 4.3), local values of $Y_{C_2H_2}$ are needed. In a di-

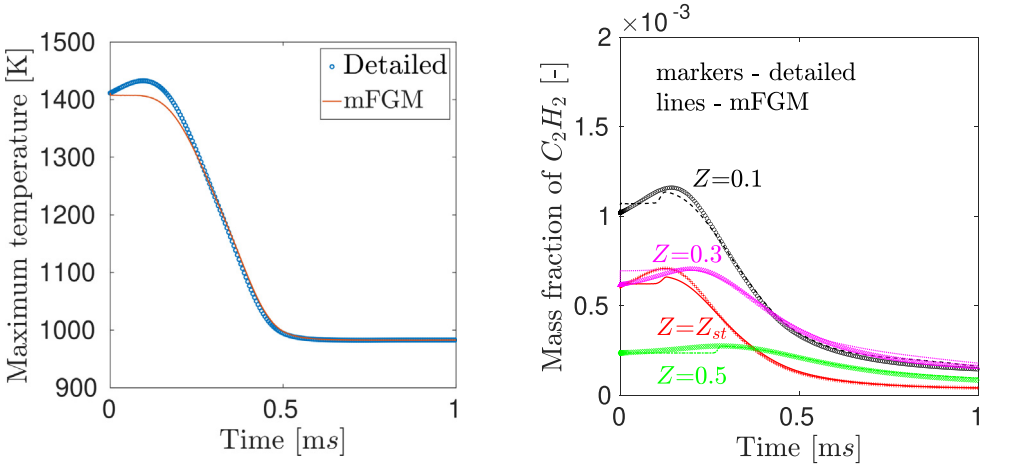

(a) Temperature

(b) Change of mass fraction of C_2H_2 with time at representative mixture fraction

Fig. 16. The progress from the unsteady branch at a =5000 s^{-1}, detailed and mFGM. The non-igniting case.

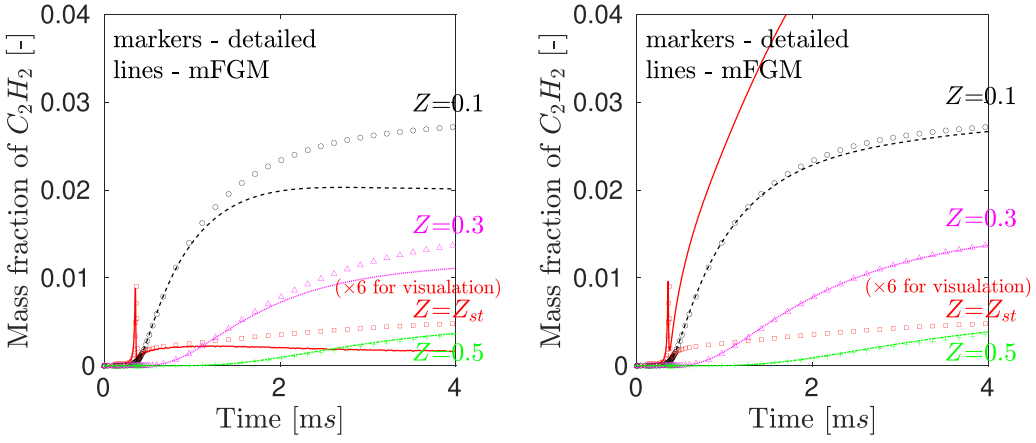

(a) FGM, direct retrieval

(b) FGM, transportation

Fig. 17. Comparison of mass fraction of acetylene between detailed chemistry and mFGM. The mass fraction at Z_{st} is amplified to 6 times of the original one.

rect retrieval method they are obtained directly by lookup in the FGM database. This might not be sufficiently accurate because the build up of $\widetilde{Y}_{C_2H_2}$ transportation (Eq. (21)) can be different from what is represented by the CD flame. In an alternative approach as mentioned in Section 2.4 that is potentially more accurate, an extra transport equation for $\widetilde{Y}_{C_2H_2}$ (Eq. (21)) is adopted and the source term of Eq. (21) is retrieved from the FGM database. To demonstrate the sensitivity to selection of either of the two approaches (respectively denoted direct retrieval and transportation), first an a priori test is performed showing the difference that already can be seen in the simulation of transient laminar CD flame. In this case Eqs. (9), (10) and the laminar version of Eq. (21) are used. The case studied again is using the ECN Spray A conditions. Results are displayed in Fig. 17 for both methods: direct retrieval (left) and transportation (right). The result of a detailed chemistry simulation not using the FGM approach is also shown. Both methods for treating C_2H_2 show differences with detailed chemistry simulation. The transportation method agrees well compared to detailed chemistry for mixture fraction values 0.1 and higher. However, at the stoichiometric mixture fraction, a significant overprediction is observed. On the contrary, the direct retrieval method shows much better agreement at the stoichiometric mixture fraction, while at higher mixture fraction the prediction significantly deviate from the detailed chemistry result. The possible reasons behind this need further study. But this laminar test reveals that both approaches can have merit depending on the local conditions. This will be taken into account when predicting the C_2H_2 for the soot formation in the turbulent flame.

3. Spray analysis

An Eulerian-Lagrangian approach is used to compute the spray. The gaseous continuum is computed using LES. The dispersed phase is represented by parcels, exchanging mass, momentum and energy with the gaseous continuum. A parcel consists of a group of droplets sharing the same thermophysical properties.

3.1. Gaseous phase modeling

In LES the turbulence is decomposed into the large scales which are directly resolved, and the unresolved small scales that need to be modeled. The variables are written as sum of a density weighted filtered value and a fluctuation as $\phi = \widetilde{\phi} + \phi''$. The Favre filtered value is related to the Reynolds filtered value via: $\widetilde{\phi} =$

$\overline{\rho\phi}/\bar{\rho}$. The filtered governing equations including unclosed terms read:

$$\frac{\partial \bar{\rho}}{\partial t} + \frac{\partial \bar{\rho}\widetilde{u}_i}{\partial x_i} = \bar{\dot{S}}_\rho, \tag{11}$$

$$\frac{\partial \bar{\rho}\widetilde{u}_i}{\partial t} + \frac{\partial \bar{\rho}\widetilde{u}_i\widetilde{u}_j}{\partial x_j} = -\frac{\partial \bar{p}}{\partial x_i} + \bar{\rho}g + \frac{\partial \bar{\tau}_{ij}}{\partial x_j} - \frac{\partial \bar{\rho}\Gamma_{ij}}{\partial x_j} + \bar{\dot{S}}_{u,i}, \tag{12}$$

$$\frac{\partial \bar{\rho}\widetilde{Z}}{\partial t} + \frac{\partial \bar{\rho}\widetilde{u}_j\widetilde{Z}}{\partial x_j} = \frac{\partial}{\partial x_j}\left[\bar{\rho}\left(\frac{\nu}{Sc} + \frac{\nu_{sgs}}{Sc_{sgs}}\right)\frac{\partial \widetilde{Z}}{\partial x_j}\right] + \bar{\dot{S}}_Z, \tag{13}$$

$$\frac{\partial \bar{\rho}\widetilde{Y}_c}{\partial t} + \frac{\partial \bar{\rho}\widetilde{u}_j\widetilde{Y}_c}{\partial x_j} = \frac{\partial}{\partial x_j}\left[\bar{\rho}\left(\frac{\nu}{Sc} + \frac{\nu_{sgs}}{Sc_{sgs}}\right)\frac{\partial \widetilde{Y}_c}{\partial x_j}\right] + \bar{\dot{\omega}}_{Y_c}, \tag{14}$$

where ρ, u_i, p, τ_{ij} denote the density, velocity, pressure and viscous stress tensor, respectively. ν represents the kinematic viscosity, and Sc the Schmidt number. Subscript sgs refers to the subgrid scale. Γ_{ij} is the turbulent stress tensor, modeled by Eq. (15). For applying the FGM approach, scalar transport equations for mixture fraction $\widetilde{Z}$ and progress variable $\widetilde{Y}_c$ are solved for turbulence. It should be noted that temperature is directly retrieved from the FGM database and not calculated by solving an enthalpy equation.

In this work, a non-viscosity based model is used for the subgrid shear stress Γ_{ij}, arising from the filtering operation in Eq. (12), namely the dynamic structure model (DS) [50], in the modified form proposed by Tsang et al. [51]:

$$\Gamma_{ij} = c_{ij}k_{sgs} - 2\nu_{noz}\left(\widetilde{S}_{ij} - \frac{1}{3}\widetilde{S}_{kk}\delta_{ij}\right). \tag{15}$$

The first term at the right hand side of Eq. (15) represents the effect of stress by subgrid fluctuations. It is the product of a position dependent tensor and the subgrid scale kinetic energy k_{sgs}, which is obtained from an extra transport equation k_{sgs} [50,52]. The second term is added to represent effects of large strain in the flow near the nozzle. It is the product of an artificial kinematic viscosity ν_{noz} obtained from an extra transport equation [51] and the symmetric part of the resolved strain rate tensor which is given by $\widetilde{S}_{ij} = 1/2(\partial\widetilde{u}_i/\partial x_j + \partial\widetilde{u}_j/\partial x_i)$. The position dependent tensor c_{ij} given by [53]:

$$c_{ij} = \frac{2L_{ij}}{L_{kk}}, \tag{16}$$

where L_{ij} is the Leonard stress tensor $L_{ij} = \widetilde{\widetilde{u}_i\widetilde{x}_i} - \widetilde{\widetilde{u}}_i\widetilde{\widetilde{u}}_j$. The performance of the DS model used in this work was extensively evaluated via a high-speed liquid spray, a channel flow, and a planar gas jet in reference [51]. More details and features regarding the DS model can be found in the literature [13,50–52,54–56].

The variance of the subgrid fluctuations of the mixture fraction variance $\widetilde{Z}_v$ is obtained from a model transport equation:

$$\frac{\partial \bar{\rho}\widetilde{Z}_v}{\partial t} + \frac{\partial \bar{\rho}\widetilde{u}_j\widetilde{Z}_v}{\partial x_j} = \frac{\partial}{\partial x_j}\left[\bar{\rho}\left(\frac{\nu}{Sc} + \frac{\nu_{sgs}}{Sc_{sgs}}\right)\frac{\partial \widetilde{Z}_v}{\partial x_j}\right] + 2\bar{\rho}\left(\frac{\nu}{Sc} + \frac{\nu_{sgs}}{Sc_{sgs}}\right)\left|\frac{\partial \widetilde{Z}}{\partial x_j}\right|^2 - 2\bar{\rho}\widetilde{\chi}, \tag{17}$$

where $\widetilde{\chi}$ is the scalar dissipation rate. $\widetilde{\chi}$ indicates the rate at which the variance of mixture fractions decays by mixing. It can be decomposed into a resolved part and a subgrid part [57]:

$$\bar{\rho}\widetilde{\chi} = \bar{\rho}\widetilde{\chi}_{res} + \bar{\rho}\widetilde{\chi}_{sgs}. \tag{18}$$

The resolved part is directly computed from the filtered mixture fraction as $\widetilde{\chi}_{res} = \nu/Sc|\nabla\widetilde{Z}|^2$, while the subgrid part is closed by $\widetilde{\chi}_{sgs} = \nu_{sgs}/Sc_{sgs}\Delta^2 Z_v$ according to the local equilibrium hypothesis [58]. Δ is the filter size.

3.2. Spray modeling

The liquid phase is solved following the standard Discrete Droplets Model (DDM) [59]. The so-called "face-to-face" method [60] is used for parcel tracking, while a "four-way coupling" is adopted by considering not only the interactions between the turbulence and particles but also the collisions between droplets [61].

A Rosin-Rammler distribution is used to represent the droplet size distribution of the injected fuel. The breakup is modeled by the Kelvin-Helmholtz and Rayleigh-Taylor (KH-RT) instabilities, where a confined length for RT instabilities is added in OpenFOAM following Ricard et al. [62].

The momentum coupling between gaseous and liquid phase is realized through the drag force using a spherical drag model [63]. The drag force term appears in the source term of both the resolved momentum Eq. (12) and the equation for the sgs kinetic energy. The drag force is function of the relative velocity U_{rel} between liquid droplet and gas. The velocity of the gas is the sum of the resolved velocity (interpolated to the particle position) and an sgs fluctuation velocity. Following Tsang et al. [52] this fluctuating component is determined from an assumed probability density function of the subgrid scale velocity fluctuations, which are assumed to be isotropic. It is written as a linear combination of the expected value u_{sgs} and a stochastic contribution u_{sto}:

$$u' = C_{sgs}u_{sgs} + u_{sto}. \tag{19}$$

The Approximate Deconvolution Model (ADM) [64], $u_{sgs,i} = 2\tilde{u}_i - 3\tilde{\tilde{u}}_i + \tilde{\tilde{\tilde{u}}}_i$, is used to reconstruct u_{sgs}. The variance needed to obtain the stochastic contribution is obtained from $\sigma^2 = 2/3C_{sig}k_{sgs}$. C_{sgs} and C_{sig} are two model constants. In the DDM the two parts have different simulation time-steps. The sgs dispersion contribution u_{sto}, is considered to be a piecewise-constant function of time. Its value changes after each time interval of length t_{turb}, a typical time scale of changes in subgrid gas fluid velocity "seen" by particles. Tsang et al. [52] proposed a new approximation of t_{turb} specifically for LES:

$$t_{turb} = C_{turb}\frac{2\Delta}{|u_{sgs} - u_d|}, \tag{20}$$

where C_{turb} is a model constant. In the new dispersion formulation, the physical meaning of t_{turb} is actually the time used for a droplet to cross the largest unresolved eddy. For more detailed discussion on model features, including the sensitivity of dispersion model constants, we refer to reference [52].

The mass and heat transfer at the droplet surface is modeled using the Ranz and Marshall correlation [65].

3.3. CFD algorithm and numerical schemes

The computational tools for solving the LES transport equations are built upon the standard spray combustion solver, sprayFoam, from the open-source CFD package—OpenFOAM [35]. New classes are created within the combustion module for the FGM storage and retrieval algorithms. The Lagrangian and turbulence libraries are also updated according to the theories mentioned in Sections 3.1 and 3.2. The PISO (Pressure Implicit with Splitting of Operator) algorithm is used for pressure-velocity correction [66]. The transport equations for mixture fraction and progress variable are solved after the velocity prediction (Eq. (12)), followed by an FGM routine to provide their sources and the necessary combustion information, temperature, laminar diffusivity, species mass fractions, etc. The PISO loop is then carried out to satisfy mass conservation. The implicit second-order backward-differencing time scheme is adopted for temporal integration, in conjunction with a cubic central differencing for the convection in momentum equation as suggested in reference [67]. Variable time-stepping is used

in the current study, where the time-step is automatically calculated each CFD time-step based on the evaluation of convection, diffusion, and the speed of sound to limit the maximum Courant-Friedrichs-Lewy (CFL) number (0.3 in this case). All Laplacian schemes are second-order, using linear central differencing. The convective terms, apart from that in momentum equation, are discretized by Normalised Variable Diagram-scheme (NVD), the Gamma differencing [68], which is a blend of first- and second-order approach, a first-order upwind scheme and a central differencing scheme, respectively.

4. Spray simulation

A first step towards an LES is the construction of an appropriate mesh. In this work, a commonly adopted 3-D cylindrical mesh, that is widely applied and extensively validated within the framework of the ECN Spray A configuration, is used [25,69,70]. The height is 108 mm which corresponds to the heigth of the Sandia constant-volume combustion chamber. The diameter is 47 mm, which is wide enough for the spray development. Boundary conditions for all faces are set to zero-gradient. A gradually expanding hexahedral mesh is applied. The smallest cell size is of 0.7 times the nozzle diameter (62.5 μ) near the nozzle, following the recommendation given in literature for modeling ECN Spray A using Lagrangian particle tracking [71,72]. Expansion ratios of 1.015 and 1.01 are taken for radial and axial directions, respectively. This leads to a total of 3.6 million cells. More details regarding the mesh can be found in reference [25,69,70]. Using the current modeling approach, the computational cost for non-reacting and reacting spray until 5 ms after the start of injection are 47 and 99 h, respectively when 128 processors are used.

4.1. The inert spray

The spray modeling is based on the methodology described in Sections 3.1 and 3.2. The performance is first validated for the non-reacting case (the inert spray, i.e. 0% O_2). The prediction with the optimized model parameters are shown in this section and these parameters are also used in the igniting case. It should be noted that, the time-averaged gaseous phase quantities, such as mixture fraction, are found to be very sensitive to the dispersion modeling. Both the randomness of Lagrangian particles and the magnitude of SGS dispersion are controlled by the model parameters selected. Our study showed that a difference in dispersion prediction affects the time needed for the spray to develop, while the time-averaged mixture fraction in the quasi-steady state is quite similar. SGS dispersion can have a significant effect on soot formation as soot development is sensitive to local transient combustion.

Figure 18 shows the prediction of global quantities. The vapor penetration is defined as the maximum distance from the nozzle outlet to the axial locations where $Z = 0.001$ is found, while the liquid penetration is defined as that of the maximum distance containing 90% of the injected liquid. Both of them are in good agreement with the Sandia experiment. Note that the experimental liquid penetration shown corresponds to a short-injection case, but it reaches a steady value quickly which is not different from that of a longer injection.

The predictions for the time-averaged temperature, mixture fraction and its variance along the spray-axis are captured well as is shown in Fig. 19.

Radial distributions of mixture fraction and temperature are given in Fig. 20. The properties are obtained from a single LES realization by azimuthal averaging the time-averaged field. The azimuthal average is realized by averaging 360 slices around the spray axis. The radial distributions at both 25 mm and 50 mm from the nozzle outlet (the end of the experiment) are well predicted. The prediction in the far field is significantly improved by using the LES-type SGS dispersion model.

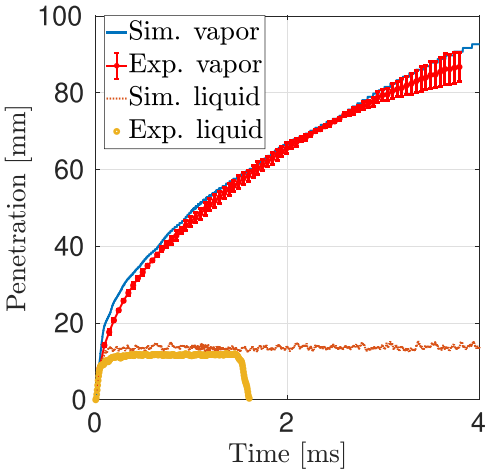

Fig. 18. A comparison of predicted and simulated liquid and vapor penetration (Spray A [73]).

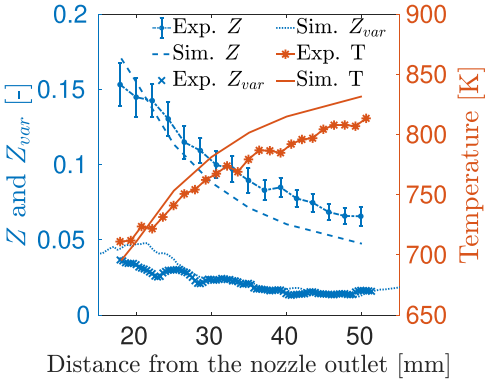

Fig. 19. The time-average quantities of the quasi-steady state on the centerline given by the turbulence model.

4.2. The reacting spray

Three different FGM strategies will be compared in the application to the igniting spray. Case 1 is the typical 2-D FGM which uses the igniting flamelet at 500 s^{-1} strain rate, i.e. FGM_{500}. Both Case 2 and Case 3 use the same set of igniting flames. Case 2 applies χ_{Anal} to identify the strain rate, whereas Case 3 applies the tabulated one that is explicitly computed according to the development of the flamelet in physical space (χ_{SSFE}) as described in 2.3.1. The transport equations for filtered controlling variables, $\widetilde{Z}$ and $\widetilde{Y}_c$, are solved following Eqs. (13) and (14).

In the case of turbulent flame, turbulence-chemsitry interaction (TCI) incorporates the effect of unresolved turbulent fluctuations on resolved chemistry. Employment of TCI in modeling turbulent combustion has been successfully applied for various configurations [75]. Specifically, in the framework of RANS, a variety of investigations regarding reacting sprays in engine-like conditions suggest a case-dependent role of TCI on combustion. Bhattacharjee and Haworth [8] observed different performance of TCI on *n*-dodecane and *n*-heptane flames, and pointed out that TCI is more crucial at lower ambient temperature. Pei et al. [76] concluded that ignition prediction is insensitive to TCI when studying an *n*-heptane spray. In later work by D'Errico et al. [18], the insensitivity was attributed to the low SDR experienced during ignition when the liquid penetration is significantly lower than the vapor

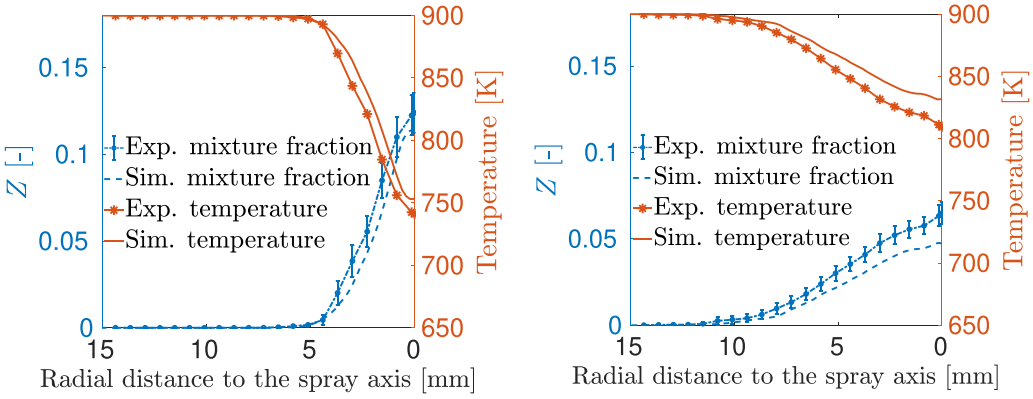

Fig. 20. The comparison of experimental and time-averaged radial mixture fraction regarding the inert Spray A case [74].

penetration, i.e. small nozzle diameter and high injection pressure which is the case studied in the present work (standard Spray A condition). Flame stabilization, on the other hand, is found to be more sensitive to the turbulent fluctuations, especially in less reactive conditions [9]. However, in the context of LES, TCI is not expected to be as important as in RANS because of the fact that unsteady motion and turbulence is resolved [77]. Regarding standard Spray A condition, great efforts have been made by applying the first order hypothesis, i.e. the well-mixed model [15,16,77–80]. For this condition, it is argued that mesh resolution plays a more primary role than TCI [15,16,37,79]. Indeed, Fulton et al. [81] demonstrated that TCI only plays a minor role within the high SDR region when the mesh is refined enough, and suggested the average mesh size to be on the order of the laminar flame thickness for resolving the flame structure. Kahila et al. [16] adopted a factor of 0.6-1.6 to define the grid spacing when simulating ECN Spray A condition and obtained good results. The current applied mesh has grid sizes of 0.23 mm and 0.36 mm at 17 mm (approximately around the flame stabilization) and 30 mm downstream from the injector orifice, respectively. As the laminar non-premixed CD flame calculations in Section 2.2 suggest a flame thickness of 0.4 mm, the mesh is considered to be fine enough. Besides, analysis of the energy spectrum for the currently adopted mesh was carried out by Desantes et al. [25]. The spectrum corresponds to the -5/3 slope in the main reaction region until a frequency of 10^6 Hz. This satisfies the inertial mesh criterion (10^4 to 10^5 Hz) according to the classic turbulence theory [82]. Hence, in this paper, we assume that at the current resolution used, TCI effects are significantly less than the effects of improved scalar dissipation rate modeling. Besides, the flamelet approach partially includes the effect of flow on chemistry by incorporating the scalar dissipation rate, which weakens the influence of TCI. As this article mainly focuses on the role of scalar dissipation rate in an igniting system, this work only considers the resolved scalar variables and ignores the subgrid effects. In other words, the PDF of all controlling variables is assumed to be a Dirac δ-function.

4.2.1. Ignition and lift-off

The ignition delay time IDT and flame lift-off length LOL are the two most important global parameters in engine applications. Generally, IDT is defined as the time when 2% of the maximum mass fraction of OH in computational domain is reached [4]. Payri et al. [36] defined the ignition for cool flame and high temperature combustion as the time spent for temperature to rise 30 ($\Delta T = 30$) and 400 ($\Delta T = 400$) K from the initial mixing line temperature, respectively. Here initialization of cool flame is refferred to as IDT_1 and the high temperature combustion as IDT_2. The cool flame period occurs between IDT_1 and IDT_2. Prediction of IDT_1 and IDT are shown in Table 3. Although previous work showed that the IDT is highly dependent on the mechanism used [34], it is seen that the scalar dissipation rate affects the IDT as well. The IDT is closer to the experiment when scalar dissipation is taken into account. The ignition can also be illustrated by the temperature rise (Fig. 21). The temperature profile clarifies that the first stage of ignition is significantly different from that in a 1-D flamelet simulation. The oscillations in this stage (around 0.25 ms) are a numerical artefact arising from the fact that Eulerian-Lagrangian constrains mesh refinement (presence of too large liquid mass fraction in a small computational cell) [83]. Local excessive liquid volume fraction especially near the nozzle outlet may lead to rapid change in temperature in an ignition simulation. However, this can be ignored since this only happens in a limited number of cells. We note that the effect is less when introducing TCI. The three different FGM

Table 3
Comparison of IDT.

Case	Case 1	Case 2	Case 3	Experiment
IDT [ms]	0.340	0.336	0.408	0.39-0.44
IDT2 [ms]	0.314	0.311	0.337	-

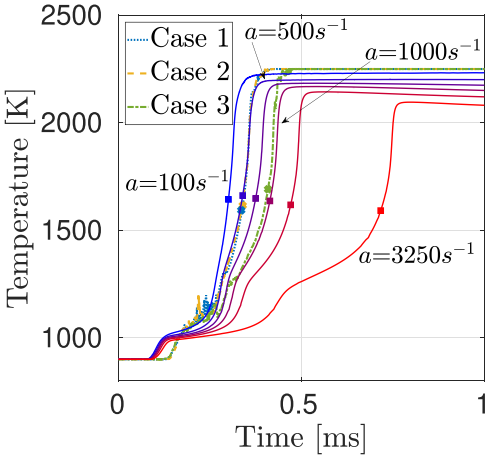

Fig. 21. The change of maximum temperature in the computational domain in time. Solid lines are ignition of 1-D flamelets with different strain rate, whose IDTs are marked by squares (■). The IDTs of the 3-D are indicated by x-marks (x).

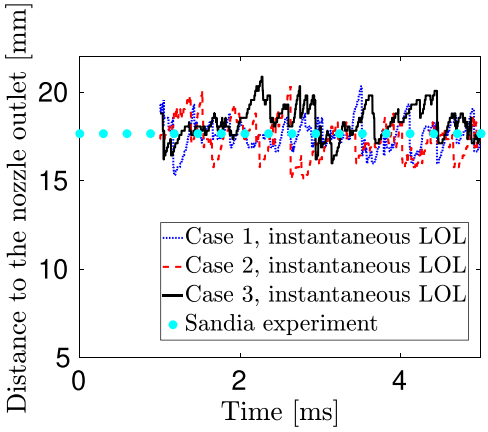

Fig. 22. The LOL predicted by different FGMs compared to the experiment.

approaches perform similarly in this stage. It was previously considered that IDT prediction in turbulent flame depends more on chemistry rather than the strain rate applied for tabulation [34,84]. However, this work suggests that the second-stage ignition is significantly influenced by the specific FGM implementation. In Case 2 (applies analytic scalar dissipation approximation χ_{Anal}), the LES prediction is similar to that of Case 1 (the single strain rate FGM, i.e. FGM_{500}) and that of the flamelet at strain rate 500 s^{-1}, i.e. the flamelet that defines the FGM_{500} table. Clearly, the application of the explicitly retrieved scalar dissipation rate χ_{SSFE} (Case 3) has an effect on the later-stage of ignition in terms of temperature.

The LOL characterises the stabilization of the flame. Evaluating the instantaneous OH field can predict the fluctuations of LOL for various boundary conditions [70]. In this paper, the instantaneous LOL at a certain time instance is determined from analysis of data on a set of transverse planes at different axial distances from the nozzle outlet. For each distance, the average of the instantaneous OH mass fraction is calculated (represented by $OH_{ave,surfi}$). The instantaneous LOL is thus the smallest axial distance from the nozzle outlet with $OH_{ave,surfi}$ reaching 2% of the maximum value among all. The LOLs obtained using different FGM approaches are shown in Fig. 22. The time-average of the instantaneous LOL for the three simulated cases is 17.5, 17.4, and 18.3 mm, respectively, and 17.7 mm in experiments. All approaches provide reasonable results and no clear distinction between them can be observed.

Formaldehyde (CH_2O) is an important intermediate species as its formation corresponds to the first stage of ignition. The qualitative comparison of CH_2O between the experiment [85] and simulation is shown in Fig. 23. Slices along the spray axis are analyzed. The slices are colored by the mass fraction of CH_2O at several representative time instances. The difference between CFD simulations is mainly seen at the time instances up to the IDT. At 0.2 ms, CH_2O for Case 1 and Case 2 extends further downstream than Case 3. This correlates with the earlier IDT predicted by Case 1 and Case 2. At 0.4 ms (around IDT and before the quasi-steady state), the field of CH_2O for Case 3 shows a wider distribution. It must be noted that all images are from a single realization. However, the trend is not expected to be changed by considering more realizations.

Fig. 24 shows the scatter plots of mixture fraction and CH_2O at several time instances, corresponding to (i) early stage of ignition, (ii) around IDT and before the quasi-steady state, (iii) early quasi-steady state, and (iv) 2 ms. Colors indicate the axial distance from the nozzle outlet. The very early ignition kernels (t=0.2 ms) lead to a very similar distribution of CH_2O in mixture fraction space. This

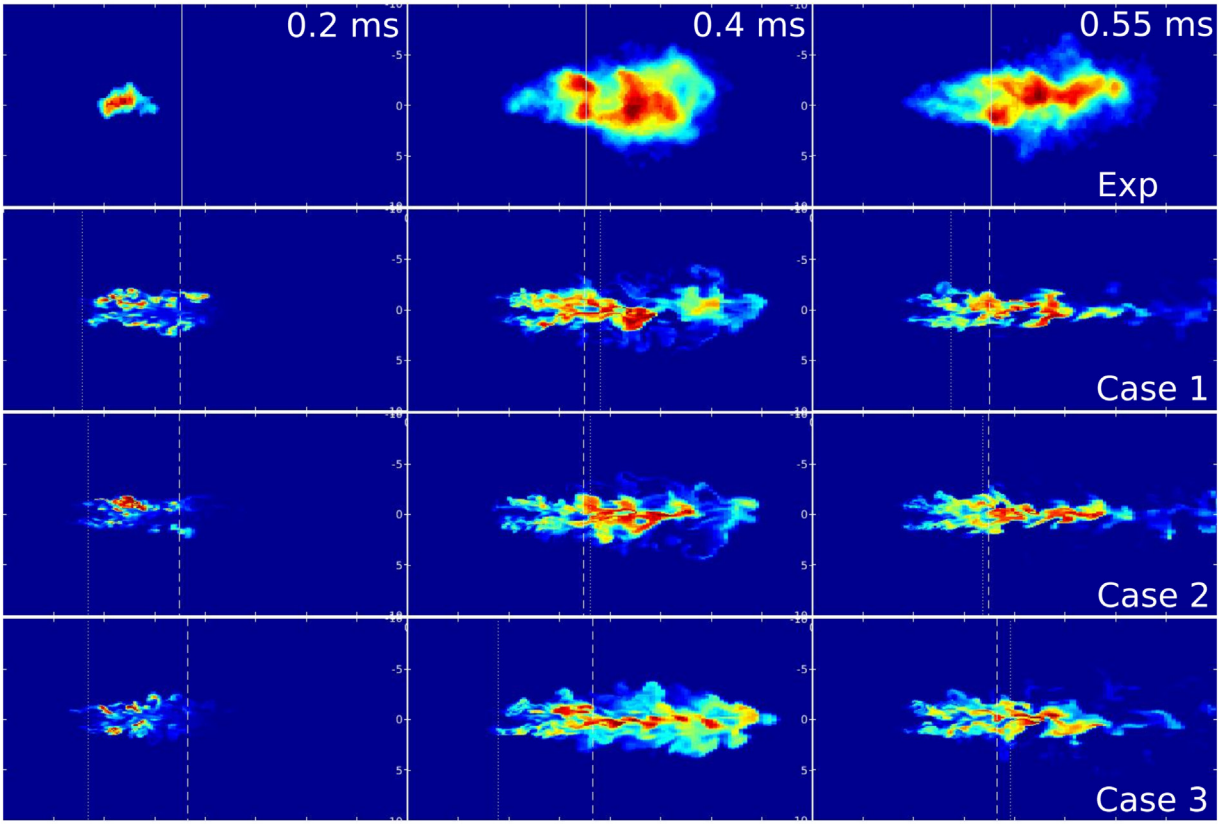

Fig. 23. A comparison of formaldehyde PLIF experiment [85] and different FGMs at representative time instances. First row: the experiment. Second row: Case 1. Third row: Case 2. Fourth row: Case three. First column: 0.2 ms. Second Column: 0.4 ms (close to ignition). Third column: 0.55 ms. Solid lines indicate the experimental LOL. Dotted lines are the instantaneous LOL. Dashed lines are the time-average of instantaneous LOL.

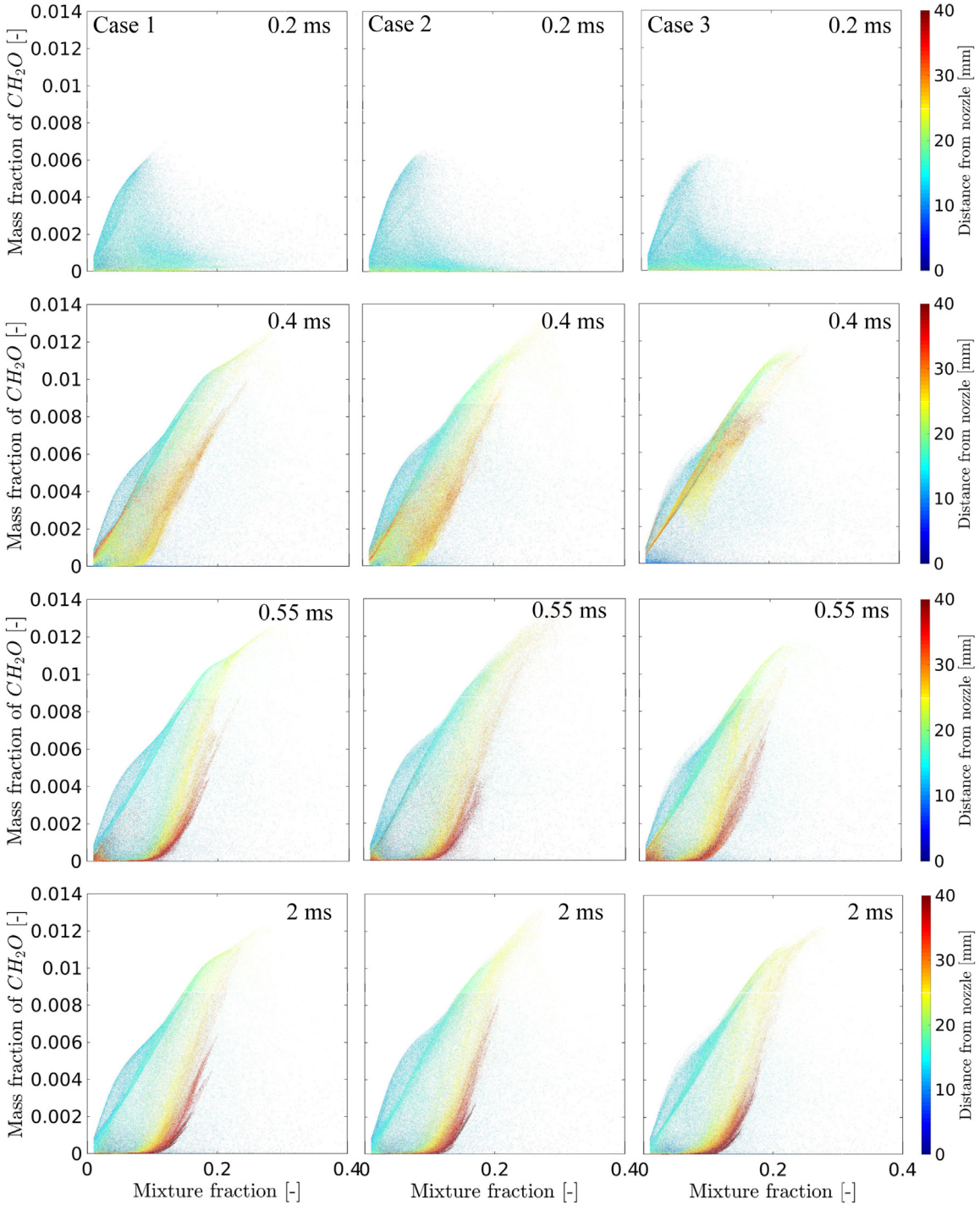

Fig. 24. Scatter plots of mixture fraction and formaldehyde, colored by the axial distance from the nozzle outlet. Blue color indicates the axial distance of 0 mm and the scatters further than 40 mm axial distance from the nozzle outlet are colored by red. From the top to the bottom: 0.2, 0.4, 0.55, and 2 ms. First column: Case 1, second column: Case 2, third column: Case 3.

corresponds to the fact that the spray development in this stage is dominated by mixing rather than the combustion model applied. At 0.4 ms, however, using χ_{SSFE} in the FGM (Case 3) results in more CH_2O at richer mixtures. Dahms et al. [47] incorporated the turbulence information in a flamelet approach and pointed out the importance of the SDR in capturing the so-called "cool flame wave". It was pointed out that the neglect of TCI using the well-mixed combustion model fails to capture this cool flame wave and does not predict first-stage ignition in rich mixtures. It is seen in Fig. 24 that by including the SDR in FGM, such ignitions in richer mixtures ($Z > 0.1$) can be achieved through χ_{SSFE}. This is not the case for typical FGM (Case 1) and the FGM applying χ_{Anal} (Case 2). Besides, the magnitude of CH_2O mass fraction for Case 3 implies a significant higher chemical reactivity than the other two cases in the spray head (>25 mm downstream of the nozzle outlet, corresponding to green and red colors). This also aligns with the observation by Dahms et al. [47]. Although maximum temperature for Case 1 and Case 2 stop evolving before 0.4 mm, a significant difference of CH_2O on mixture fraction is seen between 0.4 ms and the quasi-steady state. After 0.55 ms, the CH_2O distribution for all

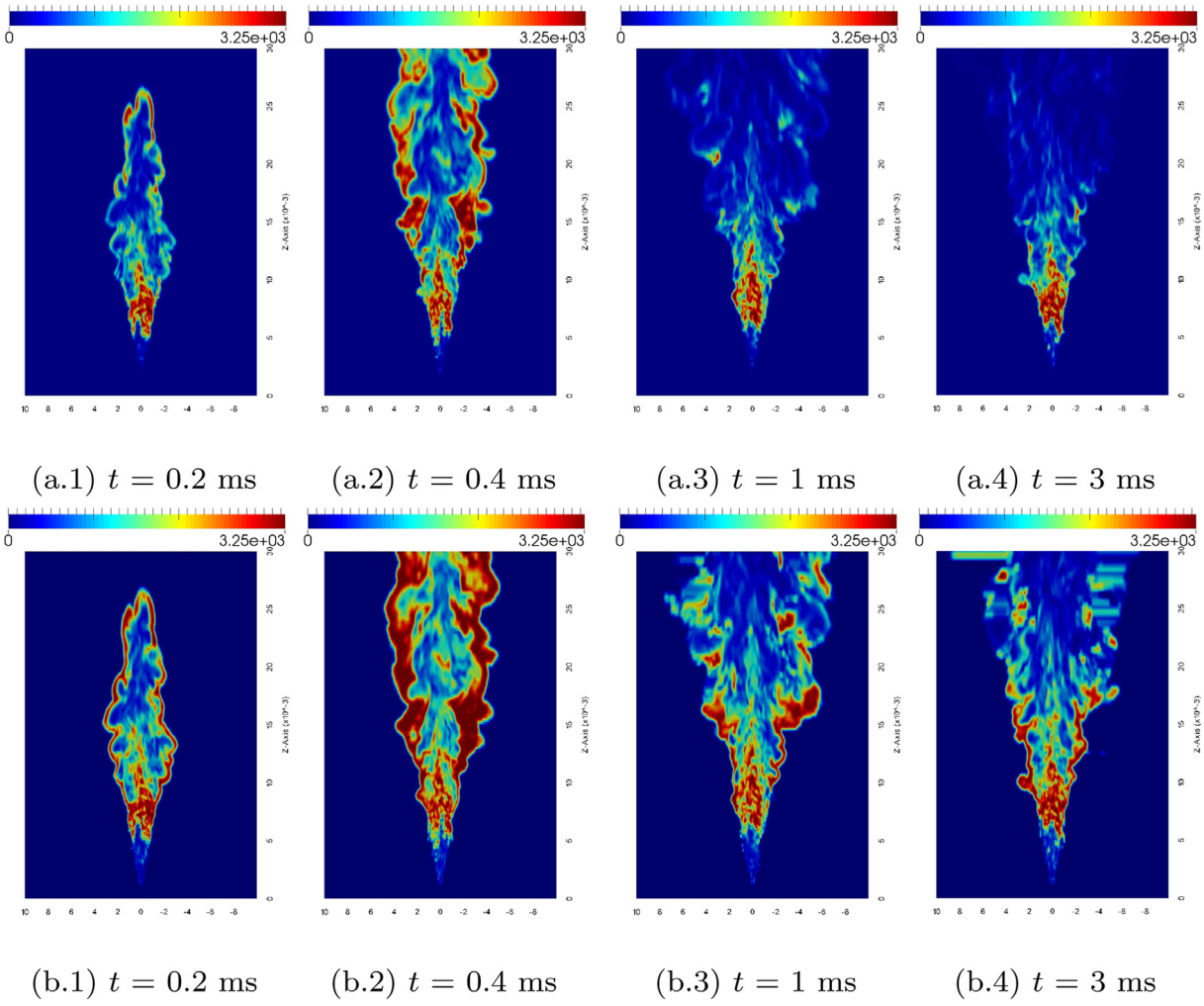

Fig. 25. Instantaneous strain rate predicted by the analytical expression (top) and the tabulated values (bottom), respectively. From the left to the right: 0.2, 0.4, 1, 3 ms.

cases remain similar. No significant difference is seen among three cases.

4.2.2. The flow structure

As the strain rate is of importance in the context of the FGM approach, it is evaluated for the two different approaches (χ_{Anal} and χ_{SSFE}, i.e. Case 2 and Case 3, respectively) in Fig. 25.

It is clear that for all time instances, the strain rate provided by the two approaches are different. Overall, Case 3 shows more variations of strain rate than Case 2 in the vicinity of flame and in the spray head. As is seen in Fig. 2(d), igniting flamelets at higher strain rates correlate with first-stage ignitions in richer mixtures. This explains the wider distributed CH_2O in mixture fraction space for Case 3 as seen in Fig. 24. For other combustion models, this wider distribution is mostly achieved via TCI [47]. Only near the nozzle outlet the starin rate values are quite similar for the two cases. This explains why the major difference is found in the second-stage ignition. The greater difference exists in the downstream region of the lift-off length, corresponding to the region where soot is produced. The new extended FGM is thus expected to have a large effect on the prediction of soot.

As is mentioned in Section 2.3, in turbulent applications, local flame states may exist in region II (Fig. 6) due to a rapid change of SDR. Indeed, a quantitative analysis shows that 1.65% and 0.91% of the flame (defined by $Z > 0.001$) by volume are in region II at 2 ms and 3 ms, respectively for Case 3. Spatially, these flame states distribute in the spray head.

4.3. Soot prediction

As mentioned earlier (Section 2.2), the prediction of C_2H_2 in the laminar flamelets is sensitive to the applied strain rate. Here the implications for soot formation modeling are presented. The Leung

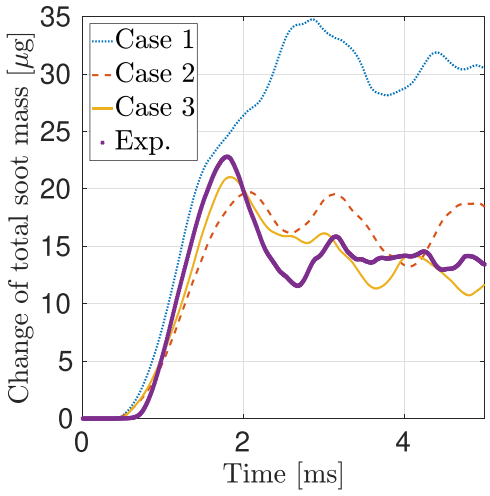

Fig. 26. Comparison of experimental total soot mass and predictions over the whole computational domain.

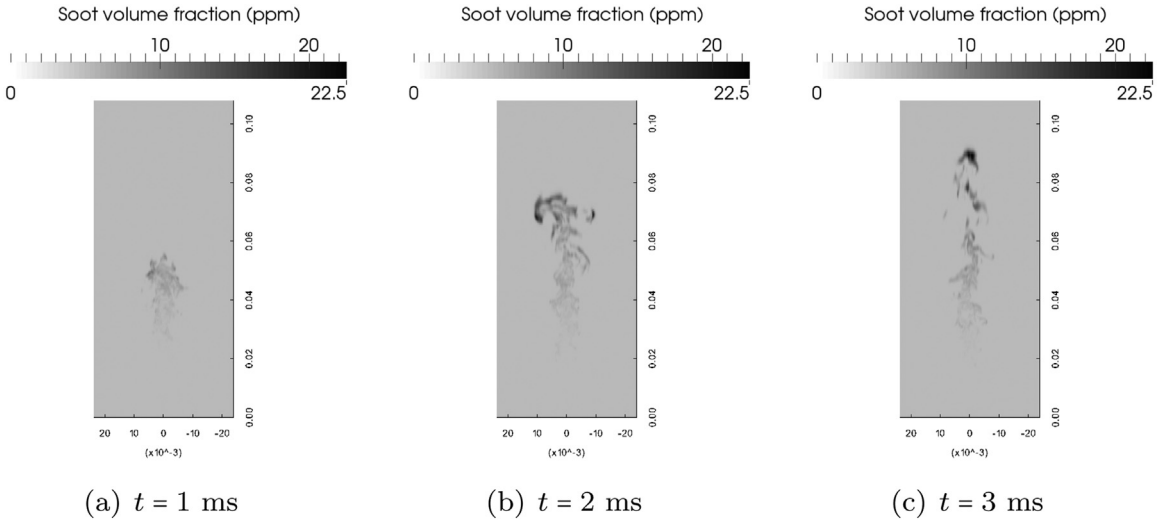

Fig. 27. Instantaneous soot volume fraction fields at different time instances given by the new extended mFGM (Case 3).

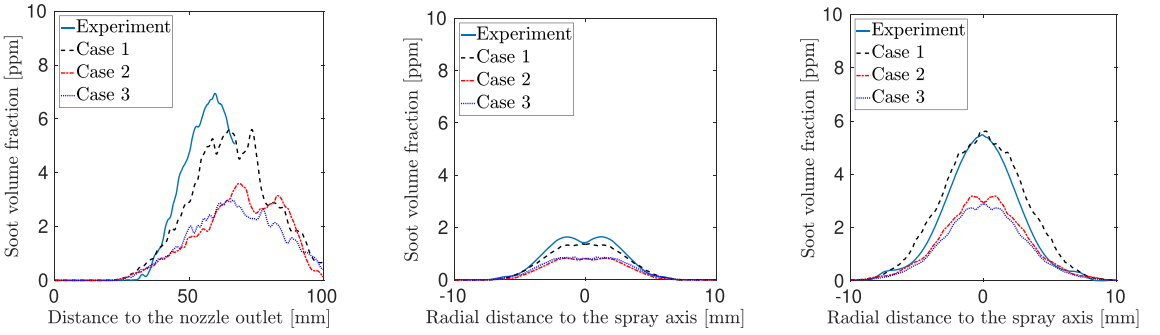

Fig. 28. Profiles of time-averaged soot volume fraction.

[86] soot model is used. The extra transport equation solved in addition to the equations for mean and variance of mixture fraction and progress variable is:

$$\frac{\partial \bar{\rho}\widetilde{Y}_{C_2H_2}}{\partial t}+\frac{\partial \bar{\rho}\widetilde{u}_j\widetilde{Y}_{C_2H_2}}{\partial x_j}=\frac{\partial}{\partial x_j}\left[\bar{\rho}\left(\frac{\nu}{Sc}+\frac{\nu_{sgs}}{Sc_{sgs}}\right)\frac{\partial \widetilde{Y}_{C_2H_2}}{\partial x_j}\right]+\bar{\dot{\omega}}_{Y_{C_2H_2}}. \quad (21)$$

$\bar{\dot{\omega}}_{Y_{C_2H_2}}$ describes the change due to gas phase chemistry.

It was found in Section 2.5 that for a laminar flame solving a transportation to obtain C_2H_2 works well for $Z > 0.07$ whereas around Z_{st} direct retrieval works better. Based on this, a simple ad-hoc procedure would be to use the two methods in the cases where they perform best, i.e. distinguish the evaluation on the local Z value. Since we neglect TCI this would extend to local $\tilde{Z}$ value, and we could use transport for $\tilde{Z} > 0.07$ and direct retrieval of mass fraction of C_2H_2 otherwise. But switching between both leads to a local discontinuity in the mass fraction field, and therefore a slightly different approach is chosen. In this approach the transport equation Eq. (21) is used in the whole domain. When $\tilde{Z} > 0.07$ the source term $\bar{\dot{\omega}}_{Y_{C_2H_2}}$ is directly retrieved from the table. Otherwise, the source term $\bar{\dot{\omega}}_{Y_{C_2H_2}}$ is first calculated from retrieved values of C_2H_2 using the transport equation as a predictive equation for the source term. Then the transport equation is used to find a final prediction of C_2H_2.

The predicted total soot mass in the computational domain by applying this "corrected" C_2H_2 source in the LES simulation is shown in Fig. 26. It is seen that by using the same soot model parameters, FGM_{500} results in a two-fold increase in soot production, compared to mFGM. Applying χ_{Anal} is comparable in the rising stage but starts to deviate in the later phase. It is noted that the reduction of total soot mass after the initial peak found in the experimental data is not only due to the oxidation in the later stages of combustion, but also due to the restricted optical access to the flame zone. The farther downstream region of the flame cannot be fully measured by experiment (as is mentioned by Maes et al. [87] for Spray C and D, and was overcome by the "forced field-of-view" method), while in the simulation the whole flame is taken into account. This can be seen in Fig. 27, where contour plots of soot volume fraction (ppm) at different time instances for Case 3 are shown. It is clearly shown that the soot formation keeps evolving towards the downstream after "quasi-steady" state with respect to temperature. Oxidation of soot does not consume all the soot formed. The total soot mass is thus expected to keep on accumulating after 2 ms and the reduction of soot formation seen in Fig. 26 must be carefully treated. The soot volume fraction in upper-stream region (between 30 and 70 mm) is relatively stable.

The ECN provides an ensemble time-averaged soot volume fraction over the quasi-steady period [88]. The predictions by the three different FGM approaches and the experimental results are shown in Fig. 28. The simulated soot volume fraction is averaged between 3 and 5 ms after start of injection. A significant difference is seen

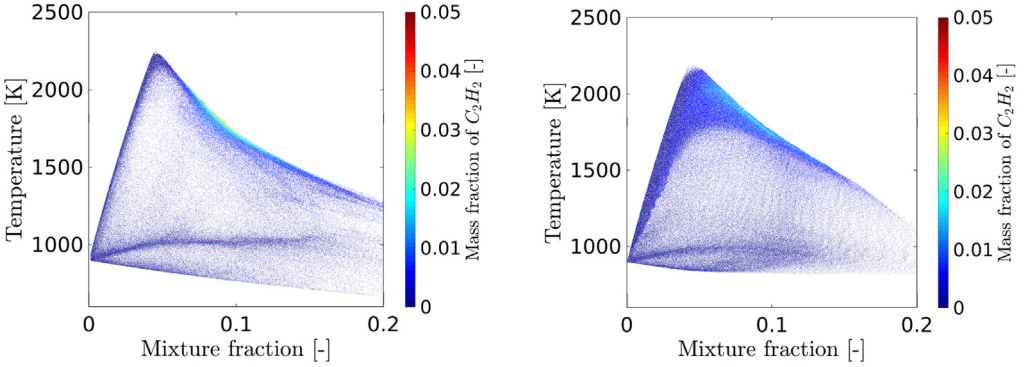

Fig. 29. Scatter plots of mass fraction of acetylene in mixture fraction and temperature space, obtained from Case 3.

for Case 1 in soot volume fraction distribution. It is seen that applying FGM_{500} predicts more soot than Case 2 and Case 3. This shows the importance of the inclusion of strain rate effect in FGM. Unlike for prediction of ignition, applying χ_{Anal} does not yield significant differences in soot volume fraction for the quasi-steady stage, especially in the upstream region. This can be attributed to the low SDR experienced for the case studied in this work, as is mentioned in Section 1. More differences are expected for a higher SDR configuration. Although the result is restricted to a single realization, the observed difference proves the importance of including the SDR effect. It is especially for the soot prediction that mFGM outperforms the single strain rate FGM.

Fig. 29 shows the scatter plots of C_2H_2 mass fraction in mixture fraction and temperature space (Case 3). Fig. 29(a) displays instantaneous quantities at 3 ms, Fig. 29(b) gives the time-averaged quantities between 2 and 3 ms. In both figures, although the highest mass fraction of C_2H_2 appears in the richer mixtures, a high number of points occur around the stoichiometric mixture fraction, i.e. the mixtures that cannot be accurately predicted by a transport equation with the source term retrieved from the table. This shows that the correction of $\tilde{\omega}_{Y_{C_2H_2}}$ is necessary to avoid the commonly observed over-prediction of total soot mass.

5. Conclusions

In this investigation a new extended multi-strain-rate FGM model, called mFGM, has been developed. The model uses scalar dissipation rate (SDR) as an additional independent variable next to mixture fraction and progress variable, allowing to represent the local time-dependent conditions. The accuracy of the model has been checked in laminar counterflow diffusion (CD) flames. It has been demonstrated that the reduced description provided by mFGM is accurate over the complete range of cases from low strain rates to beyond the ignition limit, i.e. the "S-curve" diagram.

The use of mFGM for turbulent spray flames has been validated against data for the experimentally well-documented ECN Spray A.

The LES is made using a customized OpenFOAM solver, where FGM is coupled with a non-viscosity LES model. A recently developed SGS dispersion model that takes the effect of turbulence on particles movement into account is applied. The inert spray data have been used to validate and calibrate the turbulence models.

In the turbulent flame calculations the scalar dissipation rate distribution derived from the resolved mixture fraction field is utilized to extract data from the mFGM according to the local time-dependent conditions. The predictions of the mFGM model are compared with those of the commonly used 2-D FGM, based on a single representative strain rate. When using the mFGM two different ways of retrieving the strain rate from the scalar dissipation rate are compared. One that applies the analytical scalar dissipation approximation (analytical relation between strain rate and scalar dissipation rate, the χ_{Anal}) and one that applies the scalar dissipation explicitly from the physical igniting 1-D flamelet solution (scalar dissipation rate is a function of mixture fraction and also progress variable, the χ_{SSFE}). The results are analyzed with respect to various aspects including the ignition, some characteristic species and soot.

It is found that both the single strain rate FGM (2-D FGM) and the new extended one (mFGM) reasonably capture the LOL. However, the mFGM applying χ_{SSFE} shows difference in predicting the ignition. The maximum temperature evolution of the second-stage ignition given by 2-D FGM is found to be largely dependent on the fixed prescribed strain rate. It closely follows the trend of the underlying 1-D igniting flamelet at that prescribed strain rate.

The studied species distributions are also influenced by the chosen FGM. The 2-D FGM fails to predict ignition in relatively rich mixtures as was pointed out by Dahms et al. [47]. For the mFGM method, the handling of scalar dissipation rate has a significant effect. The mFGM using χ_{SSFE} leads to wider distribution of CH_2O in mixture fraction space and more frequently appearing CH_2O in the vicinity of spray as well as in the upstream spray.

This effect on species predictions also affects soot predictions. This is clearly observed in both the total soot mass and soot volume fraction. Although these observations are based on a single LES realization, we expect that it will be confirmed by a study doing the averaging over many realisations.

It is concluded that the multi-strain-rate FGM shows significant improvements in predicting high pressure *n*-dodecane spray flames. Including the effect of turbulent mixing into the framework of FGM is shown to be important for the temporal and spatial development of minor species. Thus, it is considered to be essential for accurate soot predictions.

Declaration of Competing Interest

The authors declare that they have no known competing financial interests or personal relationships that could have appeared to influence the work reported in this paper.

Acknowledgments

The authors would like to thank the China Scholarship Council (CSC) (Grant No. 201707720061) for the scholarship support for the first author. The authors' deepest gratitude goes to Ricardo Novella at Universitat Politècnica de València for sharing his experience in modelling spray combustion and frequent communication.

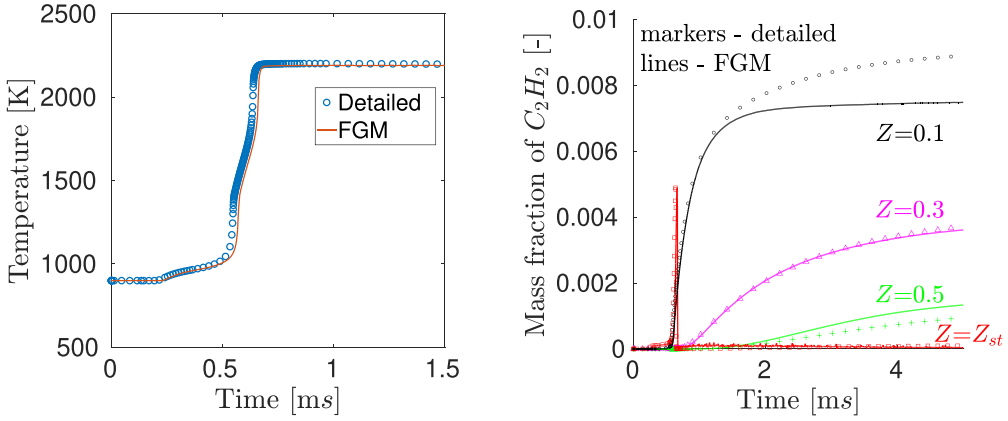

(a) Temperature rize, detailed chemistry and FGM

(b) Mass fraction of acetylence at representative mixture fraction, detailed chemistry and FGM

Fig. A.30. Performance of the new defined progress variable on temperature rise and mass fraction of acetylene.

Appendix A. Performance of the new progress variable definition in combination with the Narayanaswamy mechanism

Fig. A.30 shows the performance of the new definition of progress variable, including the soot precursor acetylene, using the Narayanaswamy mechanism. The temperature rise tendency is captured well according to Fig. A.30(a). Fig. A.30(b) illustrates that the new progress variable definition can predict the change of acetylene well for a wide range of mixture fraction.

References

[1] BP statistical review of world energy 2019, (https://www.bp.com/content/dam/bp/business-sites/en/global/corporate/pdfs/energy-economics/statistical-review/bp-stats-review-2019-full-report.pdf/). Accessed July 23, 2021.

[2] N. Maes, M. Meijer, N. Dam, B. Somers, H.B. Toda, G. Bruneaux, S.A. Skeen, L.M. Pickett, J. Manin, Characterization of spray A flame structure for parametric variations in ECN constant-volume vessels using chemiluminescence and laser-induced fluorescence, Combust. Flame 174 (2016) 138–151.

[3] R. Payri, J.M. García-Oliver, M. Bardi, J. Manin, Fuel temperature influence on diesel sprays in inert and reacting conditions, Appl. Therm. Eng. 35 (2012) 185–195.

[4] L.M. Pickett, G. Bruneaux, R. Payri, Engine Combustion Network, (https://ecn.sandia.gov/). Accessed July 23, (2021).

[5] M. Meijer, B. Somers, J. Johnson, J. Naber, S.-Y. Lee, L.M.C. Malbec, G. Bruneaux, L.M. Pickett, M. Bardi, R. Payri, T. Bazyn, Engine Combustion Network (ECN): characterization and comparison of boundary conditions for different combustion vessels, At. Sprays 22 (9) (2012) 777–806.

[6] R.D. Reitz, Directions in internal combustion engine research, Combust. Flame 160 (1) (2013) 1–8.

[7] C. Bajaj, M. Ameen, J. Abraham, Evaluation of an unsteady flamelet progress variable model for autoignition and flame lift-off in diesel jets, Combust. Sci. Technol. 185 (3) (2013) 454–472.

[8] S. Bhattacharjee, D.C. Haworth, Simulations of transient n-heptane and n-dodecane spray flames under engine-relevant conditions using a transported PDF method, Combust. Flame 160 (10) (2013) 2083–2102.

[9] Y. Pei, E.R. Hawkes, S. Kook, G.M. Goldin, T. Lu, Modelling n-dodecane spray and combustion with the transported probability density function method, Combust. Flame 162 (5) (2015) 2006–2019.

[10] Y. Zhang, H. Wang, A. Both, L. Ma, M. Yao, Effects of turbulence-chemistry interactions on auto-ignition and flame structure for n-dodecane spray combustion, Combust. Theor. Model. 23 (5) (2019) 907–934.

[11] K. Sone, S. Menon, Effect of subgrid modeling on the in-cylinder unsteady mixing process in a direct injection engine, J. Eng. Gas Turbine Power 125 (2) (2003) 435–443.

[12] X. Jiang, G.A. Siamas, K. Jagus, T.G. Karayiannis, Physical modelling and advanced simulations of gas–liquid two-phase jet flows in atomization and sprays, Prog. Energy Combust. Sci. 36 (2) (2010) 131–167.

[13] C.J. Rutland, Large-eddy simulations for internal combustion engines–a review, Int. J. Engine Res. 12 (5) (2011) 421–451.

[14] S. Som, D.E. Longman, Z. Luo, M. Plomer, T. Lu, P.K. Senecal, E. Pomraning, Simulating flame lift-off characteristics of diesel and biodiesel fuels using detailed chemical-kinetic mechanisms and LES turbulence model, Intern. Combust. Engine Div. Fall Tech. Conf. 44427 (2011) 871–882.

[15] Y. Pei, S. Som, E. Pomraning, P.K. Senecal, S.A. Skeen, J. Manin, L.M. Pickett, Large eddy simulation of a reacting spray flame with multiple realizations under compression ignition engine conditions, Combust. Flame 162 (12) (2015) 4442–4455.

[16] H. Kahila, A. Wehrfritz, O. Kaario, V. Vuorinen, Large-eddy simulation of dual–fuel ignition: diesel spray injection into a lean methane-air mixture, Combust. Flame 199 (2019) 131–151.

[17] N. Peters, Laminar diffusion flamelet models in non-premixed turbulent combustion, Prog. Energy Combust. Sci. 10 (3) (1984) 319–339.

[18] G. D'Errico, T. Lucchini, F. Contino, M. Jangi, X.-S. Bai, Comparison of well-mixed and multiple representative interactive flamelet approaches for diesel spray combustion modelling, Combust. Theor. Model. 18 (1) (2014) 65–88.

[19] J. Tillou, J.-B. Michel, C. Angelberger, C. Bekdemir, D. Veynante, Large-eddy simulation of diesel spray combustion with exhaust gas recirculation, Oil Gas Sci. Technol.–Rev. IFP Energies Nouv. 69 (1) (2014) 155–165.

[20] M.M. Ameen, J. Abraham, RANS and LES Study of Lift-off Physics in Reacting Diesel Jets, SAE Technical Pap., (2014) 2014-01-1118.

[21] M.M. Ameen, P. Kundu, S. Som, Novel tabulated combustion model approach for lifted spray flames with large eddy simulations, SAE Int. J. Engines 9 (4) (2016) 2056–2065.

[22] M. Ihme, H. Pitsch, Prediction of extinction and reignition in nonpremixed turbulent flames using a flamelet/progress variable model: 1. a priori study and presumed PDF closure, Combust. Flame 155 (1–2) (2008) 70–89.

[23] M. Davidovic, T. Falkenstein, M. Bode, L. Cai, S. Kang, J. Hinrichs, H. Pitsch, LES of n-dodecane spray combustion using a multiple representative interactive flamelets model, Oil Gas Sci. Technol.–Rev. IFP Energies Nouv. 72 (5) (2017) 29.

[24] M. Ameen, V. Magi, J. Abraham, Modeling the transient structure of reacting diesel jets using large eddy simulation, Proceeding of the 8th US National Combustion Meeting, University of Utah, 1 (2013), pp. 522–5381.

[25] J.M. Desantes, J.M. García-Oliver, R. Novella, E.J. Pérez-Sánchez, Application of an unsteady flamelet model in a RANS framework for spray a simulation, Appl. Therm. Eng. 117 (2017) 50–64.

[26] P. Kundu, M. Ameen, U. Unnikrishnan, S. Som, Implementation of a tabulated flamelet model for compression ignition engine applications, Proceedings of the SAE Technical Paper (2017).

[27] L. De Goey, J. ten Thije Boonkkamp, A flamelet description of premixed laminar flames and the relation with flame stretch, Combust. Flame 119 (3) (1999) 253–271.

[28] L. De Goey, J. ten Thije Boonkkamp, A mass-based definition of flame stretch for flames with finite thickness, Combust. Sci. Technol. 122 (1–6) (1997) 399–405.

[29] J.A. Van Oijen, A. Donini, R. Bastiaans, J. ten Thije Boonkkamp, L. De Goey, State-of-the-art in premixed combustion modeling using flamelet generated manifolds, Prog. Energy Combust. Sci. 57 (2016) 30–74.

[30] R.W. Bilger, S.H. Stårner, R.J. Kee, On reduced mechanisms for methane-air combustion in nonpremixed flames, Combust. Flame 80 (2) (1990) 135–149.

[31] Z. Sun, C. Hasse, A. Scholtissek, Ignition under strained conditions: a comparison between instationary counterflow and non-premixed flamelet solutions, Flow Turbul. Combust. 106 (4) (2021) 1277–1293.

[32] M.U. Göktolga, L.P.H. de Goey, J.A. van Oijen, Modeling curvature effects in turbulent autoigniting non-premixed flames using tabulated chemistry, Proc. Combust. Inst. 38 (2) (2021) 2741–2748.

[33] C. Bekdemir, L. Somers, L. De Goey, J. Tillou, C. Angelberger, Predicting diesel combustion characteristics with large-eddy simulations including tabulated chemical kinetics, Proc. Combust. Inst. 34 (2) (2013) 3067–3074.
[34] A. Wehrfritz, O. Kaario, V. Vuorinen, B. Somers, Large Eddy simulation of n-dodecane spray flames using flamelet generated manifolds, Combust. Flame 167 (2016) 113–131.
[35] OpenFOAM official website, (https://www.openfoam.org/). Accessed July 23, 2021.
[36] F. Payri, J.M. García-Oliver, R. Novella, E.J. Pérez-Sánchez, Influence of the n–dodecane chemical mechanism on the CFD modelling of the diesel-like ECN spray a flame structure at different ambient conditions, Combust. Flame 208 (2019) 198–218.
[37] P. Kundu, M.M. Ameen, S. Som, Importance of turbulence-chemistry interactions at low temperature engine conditions, Combust. Flame 183 (2017) 283–298.
[38] L.M. Pickett, C.L. Genzale, G. Bruneaux, L.-M. Malbec, L. Hermant, C. Christiansen, J. Schramm, Comparison of diesel spray combustion in different high-temperature, high-pressure facilities, SAE Int. J. Engines 3 (2) (2010) 156–181.
[39] K. Seshadri, F.A. Williams, Laminar flow between parallel plates with injection of a reactant at high reynolds number, Int. J. Heat Mass Transf. 21 (2) (1978) 251–253.
[40] G. Stahl, J. Warnatz, Numerical investigation of time-dependent properties and extinction of strained methane- and propane-air flamelets, Combust. Flame 85 (3–4) (1991) 285–299.
[41] C. Bekdemir, Tabulated Chemical Kinetics for Efficient and Detailed Simulations of Diesel Engine Combustion, Technische Universiteit Eindhoven, Eindhoven, 2012. Ph.D. thesis
[42] B. Somers, The simulation of Flat Flames with Detailed and Reduced Chemical Models, Technische Universiteit Eindhoven, Eindhoven, 1994. Ph.D. thesis
[43] W. Ramaekers, Development of Flamelet Generated Manifolds for Partially-Premixed Flame Simulations, Technische Universiteit Eindhoven, Eindhoven, 2011. Ph.D. thesis
[44] J.A. van Oijen, Flamelet-Generated Manifolds: Development and Application to Premixed Laminar Flames, Technische Universiteit Eindhoven, Eindhoven, 2002. Ph.D. thesis
[45] T. Yao, Y. Pei, B.-J. Zhong, S. Som, T. Lu, K.H. Luo, A compact skeletal mechanism for n-dodecane with optimized semi-global low-temperature chemistry for diesel engine simulations, Fuel 191 (2017) 339–349.
[46] B. Akkurt, Modelling Multi-Pulse Diesel Injection with Flamelet Generated Manifolds, Technische Universiteit Eindhoven, Eindhoven, 2019. Ph.D. thesis
[47] R.N. Dahms, G.A. Paczko, S.A. Skeen, L.M. Pickett, Understanding the ignition mechanism of high-pressure spray flames, Proc. Combust. Inst. 36 (2) (2017) 2615–2623.
[48] L.M. Pachano Prieto, CFD Modeling of Combustion and Soot Production in Diesel Sprays, Universitat Politşcnica de Valşncia, Valşncia, 2020. Ph.D. thesis
[49] F.N. Fritsch, R.E. Carlson, Monotone piecewise cubic interpolation, SIAM J. Numer. Anal. 17 (2) (1980) 238–246.
[50] N. Bharadwaj, C.J. Rutland, S.-M. Chang, Large eddy simulation modelling of spray-induced turbulence effects, Int. J. Engine Res. 10 (2) (2009) 97–119.
[51] C.-W. Tsang, M.F. Trujillo, C.J. Rutland, Large-eddy simulation of shear flows and high-speed vaporizing liquid fuel sprays, Comput. Fluids 105 (2014) 262–279.
[52] C.-W. Tsang, C.-W. Kuo, M. Trujillo, C. Rutland, Evaluation and validation of large-eddy simulation sub-grid spray dispersion models using high-fidelity volume-of-fluid simulation data and engine combustion network experimental data, Int. J. Engine Res. 20 (6) (2018) 583–605.
[53] M. Germano, U. Piomelli, P. Moin, W.H. Cabot, A dynamic subgrid-scale eddy viscosity model, Physics of Fluids A: Fluid Dynamics 3 (7) (1991) 1760–1765.
[54] S. Menon, Subgrid combustion modelling for large-eddy simulations, Int. J. Engine Res. 1 (2) (2000) 209–227.
[55] E. Pomraning, C.J. Rutland, Dynamic one-equation nonviscosity large-eddy simulation model, AIAA J. 40 (4) (2002) 689–701.
[56] H. Lu, C.J. Rutland, L.M. Smith, A priori tests of one-equation LES modeling of rotating turbulence, J. Turbul. 8 (2007) N37.
[57] S.S. Girimaji, Y. Zhou, Analysis and modeling of subgrid scalar mixing using numerical data, Phys. Fluids 8 (5) (1996) 1224–1236.
[58] C.D. Pierce, P. Moin, A dynamic model for subgrid-scale variance and dissipation rate of a conserved scalar, Phys. Fluids 10 (12) (1998) 3041–3044.
[59] J.K. Dukowicz, A particle-fluid numerical model for liquid sprays, J. Comput. Phys. 35 (2) (1980) 229–253.
[60] F.P. Kärrholm, Numerical Modelling of Diesel Spray Injection, Turbulence Interaction and Combustion, Chalmers University of Technology, Gŋteborg, 2008.
[61] P.J. O'Rourke, Collective Drop Effects on Vaporizing Liquid Sprays, Princeton University, Princeton, 1981.
[62] L.M. Ricart, J. Xin, G.R. Bower, R.D. Reitz, In-cylinder measurement and modeling of liquid fuel spray penetration in a heavy-duty diesel engine, SAE Trans 106 (3) (1997) 1622–1640.
[63] A.A. Amsden, KIVA-II: A Computer Program for Chemical Reactive Flows with Sprays, Los Alamos National Laboratory Report (1989), p. 11560.
[64] S. Stolz, N.A. Adams, L. Kleiser, An approximate deconvolution model for large-eddy simulation with application to incompressible wall-bounded flows, Phys. Fluids 13 (4) (2001) 997–1015.
[65] W.E. Ranz, W.R. Marshall, Evaporation from drops, Chem. Eng. Prog. 48 (3) (1952) 141–146.
[66] R.I. Issa, Solution of the implicitly discretised fluid flow equations by operator-splitting, J. Comput. Phys. 62 (1) (1986) 40–65.
[67] C.-W. Tsang, C. Rutland, Effects of numerical schemes on large eddy simulation of turbulent planar gas jet and diesel spray, SAE Int. J. Fuels Lubr. 9 (1) (2016) 149–164.
[68] H. Jasak, Error Analysis and Estimation for the Finite Volume Method with Applications to Fluid Flows, Imperial College (University of London), London, 1996. Ph.D. thesis
[69] J.M.M. Laborda, Engineering Large Eddy Simulation of Diesel Sprays, Universitat Politşcnica de Valşncia, Valşncia, 2014. Ph.D. thesis
[70] E.J. Pérez-Sánchez, J.M. Garcia-Oliver, R. Novella, J.M. Pastor, Understanding the diesel-like spray characteristics applying a flamelet-based combustion model and detailed large eddy simulations, Int. J. Engine Res. 21 (1) (2020) 134–150.
[71] Q. Xue, S. Som, P.K. Senecal, E. Pomraning, Large eddy simulation of fuel-spray under non-reacting IC engine conditions, At. Sprays 23 (10) (2013).
[72] P.K. Senecal, E. Pomraning, K.J. Richards, S. Som, An investigation of grid convergence for spray simulations using an LES turbulence model, Proceedings ot the SAE Technical Paper (2013).
[73] P.M. Lillo, L.M. Pickett, H. Persson, O. Andersson, S. Kook, Diesel spray ignition detection and spatial/temporal correction, SAE Int. J. Engines 5 (3) (2012) 1330–1346.
[74] J. Abraham, L.M. Pickett, Computed and measured fuel vapor distribution in a diesel spray, At. Sprays 20 (3) (2010) 241–250.
[75] D.C. Haworth, Progress in probability density function methods for turbulent reacting flows, Prog. Energy Combust. Sci. 36 (2) (2010) 168–259.
[76] Y. Pei, E.R. Hawkes, S. Kook, A comprehensive study of effects of mixing and chemical kinetic models on predictions of n-heptane jet ignitions with the PDF method, Flow Turbul. Combust. 91 (2) (2013) 249–280.
[77] C. Gong, M. Jangi, X.-S. Bai, Large eddy simulation of n-dodecane spray combustion in a high pressure combustion vessel, Appl. Energy 136 (2014) 373–381.
[78] M.M. Ameen, Y. Pei, S. Som, Computing statistical averages from large eddy simulation of spray flames, Proceedings ot the SAE Technical Paper (2016).
[79] C. Xu, M.M. Ameen, S. Som, J.H. Chen, Z. Ren, T. Lu, Dynamic adaptive combustion modeling of spray flames based on chemical explosive mode analysis, Combust. Flame 195 (2018) 30–39.
[80] P.C. Ma, H. Wu, T. Jaravel, L. Bravo, M. Ihme, Large-eddy simulations of transcritical injection and auto-ignition using diffuse-interface method and finite-rate chemistry, Proc. Combust. Inst. 37 (3) (2019) 3303–3310.
[81] J.A. Fulton, J.R. Edwards, A. Cutler, J. McDaniel, C. Goyne, Turbulence/chemistry interactions in a ramp-stabilized supersonic hydrogen–air diffusion flame, Combust. Flame 174 (2016) 152–165.
[82] S.B. Pope, Turbulent flows, 2001.
[83] M. Sontheimer, A. Kronenburg, O.T. Stein, Grid dependence of evaporation rates in Euler–Lagrange simulations of dilute sprays, Combust. Flame 232 (2021) 111515.
[84] U. Egüz, S. Ayyapureddi, C. Bekdemir, B. Somers, P. de Goey, Manifold resolution study of the FGM method for an igniting diesel spray, Fuel 113 (2013) 228–238.
[85] H.S. Sim, N. Maes, L. Weiss, L.M. Pickett, S.A. Skeen, Detailed measurements of transient two-stage ignition and combustion processes in high-pressure spray flames using simultaneous high-speed formaldehyde PLIF and schlieren imaging, Proc. Combust. Inst. 38 (4) (2021) 5713–5721.
[86] K.M. Leung, R.P. Lindstedt, W.P. Jones, A simplified reaction mechanism for soot formation in nonpremixed flames, Combust. Flame 87 (3–4) (1991) 289–305.
[87] N. Maes, S.A. Skeen, M. Bardi, R.P. Fitzgerald, L.-M. Malbec, G. Bruneaux, L.M. Pickett, K. Yasutomi, G. Martin, Spray penetration, combustion, and soot formation characteristics of the ECN Spray C and Spray D injectors in multiple combustion facilities, Appl. Therm. Eng. (2020) 115136.
[88] T. Xuan, J.M. Desantes, J.V. Pastor, J.M. Garcia-Oliver, Soot temperature characterization of spray a flames by combined extinction and radiation methodology, Combust. Flame 204 (2019) 290–303.